Understanding the nature of the magnetic coupling in transition metal doped Bi_2Se_3

Sagar Sarkar [1,2,*] Shivalika Sharma [1,3] Olle Eriksson,[2,4] and Igor Di Marco [1,2,3,†]
[1]*Asia Pacific Center for Theoretical Physics, Pohang 37673, Korea*
[2]*Department of Physics and Astronomy, Uppsala University, Uppsala 751 20, Sweden*
[3]*Institute of Physics, Nicolaus Copernicus University, 87-100 Toruń, Poland*
[4]*WISE, Wallenberg Initiative Materials Science, Uppsala University, Uppsala 751 20, Sweden*

(Received 19 May 2024; revised 23 July 2024; accepted 26 July 2024; published 9 August 2024)

In this paper, we employ electronic structure theory to investigate the nature of the exchange coupling in transition metal doped Bi_2Se_3. We focus on V, Cr, Mn, and Fe, which have been under scrutiny for the realization of the quantum anomalous Hall effect. For simplicity, we model the doping process as happening inside a single layer of Bi within a single quintuple layer inside a three-formula-unit conventional hexagonal cell and consider situations of full coverage or half coverage. Due to the covalent nature of the chemical bond between transition metal atoms and selenium, this simple model is capable of describing the fundamental features of the intraplane exchange coupling, while offering a clearer analysis of the response to structural, magnetic, and electronic perturbations. In agreement with recent literature, our results confirm that the van Vleck mechanism has a very marginal contribution to the exchange coupling. Depending on the filling of the 3*d* shell and on the details of the electronic structure, several other mechanisms compete and cooperate to induce the magnetic order. For V, double exchange and superexchange cooperate to have the strongest ferromagnetic coupling among the investigated elements, followed by Cr where only superexchange is active. For Mn, superexchange and double exchange compete to create an extremely weak ferromagnetic order. For Fe, a strong antiferromagnetic coupling caused by the double exchange is observed to dominate over the ferromagnetic Ruderman-Kittel-Kasuya-Yosida interaction, but the high sensitivity of this competition to the doping concentration suggests that our conclusion may not hold in the dilute limit. Overall, Fe doping seems to offer the most intriguing competition of exchange mechanisms that can be tuned by adjusting the doping concentration and the details of the host, as, e.g., by replacing Se with Te or Bi with Sb.

DOI: 10.1103/PhysRevB.110.064412

I. INTRODUCTION

The presence of quantized Landau levels in a two-dimensional (2D) electron gas under a strong magnetic field leads to a topological state of matter with zero longitudinal resistance in association with a quantized Hall conductance. This phenomenon goes under the name of quantum Hall effect (QHE) and was shown experimentally by von Klitzing [1]. While this state of matter is connected to the emergence of a band gap at the Fermi level, the boundaries or edges exhibit 1D gapless chiral edge states (CESs). These CESs are protected from back-scattering (from one edge to another), allowing for a unidirectional, dissipationless flow of current along the edges of the sample [2,3]. Hence such systems have attracted much attention from the scientific community, as suitable candidates for application in electronic devices. Even more intriguing has been the discovery that these physical properties do not necessarily require an external magnetic field, but are more fundamentally connected to the presence of protected CESs with a broken time-reversal symmetry (TRS) [2,3]. Various predictions [2,4,5] were then made about the emergence of an effect analogous to the QHE in certain 2D magnetic insulators in the absence of an external magnetic field and Landau levels, named the quantum anomalous Hall effect (QAHE) [6]. Two essential conditions were identified [5] to realize the QAHE: (i) a 2D insulating material where the ferromagnetic (FM) order breaks TRS and (ii) a band inversion transition resulting from the spin-orbit coupling (SOC) to have CESs. These conditions were also predicted to be *easily* realizable in topological insulators (TIs) doped with magnetic impurities [5]. TIs have a bulk band gap resulting from SOC along with topologically protected gapless surface states with TRS [7]. Hence, establishing FM order in a suitable TI will break the TRS and open a gap around the CES; then, if the Fermi level is adjusted to be inside the magnetically opened gap, the QAHE should be realized [8]. This prediction has been experimentally realized in Cr- and V-doped films of the tetradymite semiconductor $(Bi, Sb)_2Te_3$ [8–12]. Similarly to what happens in the QHE, dissipationless currents flow via the 1D CES even in the absence of an external magnetic field.

*Contact author: sagar.sarkar@physics.uu.se
†Contact author: igor.dimarco@physics.uu.se

This makes QAHE systems potential candidates for devices for electronics, spintronic [2,6], and quantum computing [13]. For a real device application of QAHE, the stability of the magnetic state and its topological properties with respect to the temperature is essential. Unfortunately, until now, QAHE has only been observed at very low temperatures [8,11,12,14], generally in the range of 15–30 K [15]. To reach full quantization, temperatures as low as 300 mK are required [16,17]. These are much lower than the ordering temperatures of the FM state in these systems, which are around 100 K [12,18,19]. The origin of this discrepancy is still under debate, but is clearly connected to the exchange coupling introduced by the magnetic dopants and its inhomogeneity in the sample [15]. Thus, it becomes of paramount importance to understand the microscopic origin of magnetic exchange between the dopants, its dependence on the type of impurities, and their concentration, as well as their effect on the topology of the electronic structure of the host material.

Over the last decade, several exchange mechanisms were suggested to be the cause of magnetism in transition metal (TM) doped TIs [20]. The initial prediction of QAHE in magnetically doped Bi_2Se_3 was based on the assumption that magnetism could arise without free carriers, via the van Vleck mechanism [21]. This mechanism depends on the strength of SOC, and the inverted band structure of TIs leads to an enhanced spin susceptibility [5,22]. At first, experimental evidence was provided in favor of the van Vleck mechanism in V- and Cr-doped $(Bi, Sb)_2Te_3$ [22,23], but later work based on resonant photoemission spectroscopy [24] and x-ray magnetic circular dichroism (XMCD) [25] contradicted this conclusion [26]. Moreover, theoretical studies on magnetically doped TIs with a finite carrier density at the Fermi level suggested the importance of the long-range Ruderman-Kittel-Kasuya-Yosida (RKKY) mechanism [27,28], which is also supported by experimental measurements [29] and in line with the dependence of the ordering temperature on the dopant concentration [30]. More recently, a doping concentration-dependent evolution of the exchange mechanism in V- and Cr-doped Bi_2Te_3 was reported, suggesting a crossover from the van Vleck exchange in the low doping regime to the RKKY interaction in the high doping regime [31]. *Ab initio* electronic structure calculations provided decisive evidence against the van Vleck mechanism by demonstrating that the long-range order and the strength of the exchange coupling are unaffected by the inclusion or exclusion of SOC [27,32–35]. Instead, it was shown that, for V- and Cr-doped TIs, the interaction between the doped magnetic atoms is mediated by the polarized *p*-orbital network of the host [33,34]. This polarization occurs due to the $p-d$ hybridization between magnetic dopants and the host atoms, which takes a primary role in the development of the long-range order [35]. This situation is reminiscent of the physics observed in dilute magnetic semiconductors (DMSs), where carrier-mediated ferromagnetism was connected to the RKKY interaction and the $p-d$ exchange mechanism, as, e.g., in Mn-doped CdSe/Te and Mn-doped GaAs [36–40]. An analogous, albeit short-range, interaction can develop even in the absence of carriers, following the Bloembergen-Rowland mechanism [41,42]. In analogy to DMSs, other short-range exchange interactions have been considered, due to, e.g., superexchange and double exchange [28,35,38,43]. For instance, antiferromagnetic (AFM) superexchange was suggested to drive the long-range order in Fe-doped Bi_2Se_3 [43] and Mn-doped Bi_2Te_3 [28], while FM superexchange was reported in Cr-doped Sb_2Te_3 [35]. FM double exchange was suggested to occur in Co-doped Bi_2Te_3 [28] and V-doped Sb_2Te_3 [35]. Finally, a recent work provided strong evidence of the dominating role of superexchange in Mn-doped HgTe and arguments were put forward on a similar situation happening in transition metal doped tetradymite semiconductors [42].

The previous discussion emphasizes that a more systematic approach is needed to clarify the nature of the exchange coupling in magnetic TIs. In this paper, we intend to provide such an analysis by performing a series of electronic structure calculations via density-functional theory (DFT) [44] and its extensions [45,46]. Our paper is focused on Bi_2Se_3 doped with selected TM atoms (V, Cr, Mn, Fe). To obtain the clearest possible insight into the character of the exchange coupling, we limit the doping process to one of the Bi layers within a single quintuple layer (QL) in the bulk material. Such doping creates a hypothetical 2D-like magnet inside a layered nonmagnetic TI with possible magnetic exchange interaction between the TM atoms. Although this simple 2D magnetic system does not allow for the quantitative analysis of the magnetic order of a given material, it offers a much clearer overview of the magnetic response and keeps the problem computationally feasible. By adopting a different strategy than previous literature, we focus on the changes of the long- (short-) range character of the exchange coupling with respect to the type of dopants, their position, and concentration. To obtain a more detailed analysis, we calculate the orbital decomposition of the interatomic exchange interaction [47], which is made possible by the local octahedral symmetry of the dopants in our model. Further insight is obtained by manipulating the electronic structure through a variation of the local Coulomb interaction U and analyzing the changes induced in the orbitally decomposed interatomic exchange parameters. Our calculations will demonstrate that even this simple modeling of the doping process incorporates all possible exchange mechanisms considered so far in the literature for explaining the magnetic properties of doped tetradymite semiconductors. Most importantly, our study will identify the dominant exchange mechanism for each impurity and will emphasize the peculiar behavior of Fe, whose properties change significantly when varying the concentration of dopants.

The present paper is organized as follows. After this Introduction, the methodological aspects of our work are presented in Sec. II. The results about the selection of the best methods for our analysis as assessed via the structural properties are illustrated in Sec. III. The analysis of the electronic and magnetic properties of TM-doped Bi_2Se_3 are then presented in Secs. IV and V for the full coverage and half coverage of one Bi layer inside a QL, respectively. Finally, the conclusions of this paper are discussed in Sec. VI.

II. METHODOLOGY

A. Structural optimization

For the structural optimization of our systems, the electronic structure was calculated using a projected augmented

wave (PAW) method [48,49] as implemented in the VIENNA AB INITIO SIMULATION PACKAGE (VASP) [50–53]. The local density approximation (LDA) [54–56] and generalized gradient approximation (GGA) [57] in the Perdew-Burke-Ernzerhof (PBE) realization [57,58] was considered for the exchange-correlation functional. For our layered system, the nonlocal, weak van der Waals (vdW) interactions become important to obtain good structural properties. These interactions also lead to a contraction of the unit cell volume, correcting the general overestimation observed in GGA. Hence, we also performed calculations by using the DFT-D2 method of Grimme [59], which was shown to be the most accurate for this class of systems [60]. Due to the presence of heavy elements like Bi, relativistic effects are also expected to be important for the structural degrees of freedom. Additional calculations were then performed with the inclusion of SOC, as implemented in the PAW methods in VASP [61]. The unit cell volume, shape, and internal positions of all the atoms were optimized for a minimum energy configuration until the forces were less than 10^{-3} eV/Å. A plane-wave energy cutoff of 700 eV was used in all these calculations for the primitive unit cell as well as supercells. An optimized Γ-centered Monkhorst-Pack mesh [62] of $18 \times 18 \times 18$ **k**-points was used for the rhombohedral primitive cell. For the conventional three-formula-unit hexagonal cell, a **k** mesh of $16 \times 16 \times 6$ was used. Whenever a cell doubling was done, the **k** mesh was reduced accordingly. In our magnetically doped systems, the presence of TM atoms introduces the problem of the treatment of the localized nature of the 3*d* states. To remedy the deficiencies of local and semilocal exchange-correlation functionals, we also performed calculations by means of the DFT + *U* approach. In this approach, a Hubbard-like term is introduced to describe the local Coulomb interaction between the 3*d* electrons; then this term is treated via the Hartree-Fock approximation [45,46]. In VASP, we employed the rotationally invariant formulation proposed by Liechtenstein *et al.* [63], where the double-counting was treated in the fully localized limit (FLL) [45]. Based on previous studies [64,65], the Coulomb interaction parameters U and J were chosen as 4.0 eV and 0.9 eV, respectively.

B. Electronic structure and interatomic exchange interaction

Following the structural optimization, we analyzed electronic and magnetic properties in more detail by means of the full-potential linear muffin-tin orbital (FPLMTO) method, as implemented in the Relativistic Spin Polarized toolkit (RSPt) [66,67]. Various exchange-correlation functionals were considered, at the level of LDA in the parametrization by Perdew and Wang (PW92) [68] and GGA in the parametrization by PBE [57,58] and by Armiento and Mattsson (AM05) [69,70]. As illustrated in the Supplemental Material (SM) [71], we found that LDA gives the best description of the calculated band structure of pristine Bi_2Se_3, in comparison to VASP and existing literature [7]. Hence, we will focus exclusively on LDA-PW92 calculations in the discussion of the electronic and magnetic properties obtained with RSPt. The RSPt basis set was constructed to include two energy sets, corresponding to valence and semicore states. The former included 6*s*, 6*p*, and 6*d* orbitals for Bi and 4*s*, 4*p*, and 4*d* orbitals for Se, while the latter included 5*d* orbitals for Bi and 3*d* orbitals for Se. The TM impurities were described by treating 4*s*, 4*p* and 3*d* states as valence and 3*s* and 3*p* states as semicore. Note that the distinction between valence and semicore states in RSPt is mainly formal and allows for the treatment of orbitals with the same angular character but with different principal quantum numbers [66]. For an increased accuracy, three kinetic tail energies were used, namely, −0.1, −2.3, and −1.5 Ry. For the Brillouin zone sampling, we used a Γ-centered Monkhorst-Pack mesh [62] of $14 \times 14 \times 4$ **k**-points for the conventional three-formula-unit hexagonal cell for both undoped and doped Bi_2Se_3. Upon introducing the SOC, it was necessary to increase the Brillouin zone sampling to achieve the requested convergence of energy and magnetic moments of the doped systems. Thus, **k** meshes up to $20 \times 20 \times 6$ and $26 \times 26 \times 8$ were considered for, respectively, V/Cr and Mn/Fe. As for the VASP calculations, doubling the unit cell size was accompanied by a corresponding adjustment of the **k** mesh. The DFT + *U* calculations were performed by means of the spin and orbital rotationally invariant formulation described in Ref. [72], using the muffin-tin heads as the local basis [73]. Again, FLL was used as the double-counting correction [45,46]. The remaining computational settings for DFT + *U* calculations were kept as described above for the LDA and GGA calculations.

From the converged electronic structure calculations, interatomic exchange interactions J_{ij} were calculated by mapping the magnetic excitations onto an effective Heisenberg Hamiltonian [74],

$$\hat{H} = -\sum_{i \neq j} J_{ij} \vec{e}_i \cdot \vec{e}_j, \tag{1}$$

where $\vec{e}_i$ and $\vec{e}_j$ are the unit vectors along the magnetic moment direction at sites i and j, respectively. Note that the choice of the Hamiltonian in Eq. (1) is not unique and one may often find expressions where a factor of 1/2 is added to the summation or where the unit vectors are replaced by the magnetic moment vectors [75]. It is important to keep track of these details when comparing results from different calculations or, to an even larger extent, when comparing to values extracted from experimental data. We direct the reader to recent review for a comprehensive overview of this topic, including how different definitions are related to different physical meanings that one may wish to emphasize [75]. In practical terms, the calculation of the J_{ij} in RSPt is performed by means of a generalized version of the magnetic force theorem (MFT) [76,77] accounting for correlation effects and orbital decompositions [47,74,78]. In the presence of SOC, the J_{ij} interaction acquires a tensorial form and the mapping of the magnetic excitations requires a more complex version of the Heisenberg Hamiltonian [75,79], namely,

$$\hat{H} = -\sum_{i \neq j} J_{ij} \vec{e}_i \cdot \vec{e}_j - \sum_{i \neq j} \vec{e}_i{}^T \mathbb{J}^S_{ij} \vec{e}_j - \sum_{i \neq j} \vec{e}_i{}^T \mathbb{J}^A_{ij} \vec{e}_j. \tag{2}$$

Here, the first term J_{ij} is the isotropic exchange interaction, corresponding to the one in Eq. (1), the second term $\mathbb{J}^S_{ij}$ is the symmetric anisotropic exchange interaction, and the third term $\mathbb{J}^A_{ij}$ is the antisymmetric anisotropic exchange interaction. This last term incorporates the Dzyaloshinskii-Moriya

TABLE I. Lattice constants a and c, cell volume V, Se-Bi bond lengths, and interlayer vdW gap as obtained from VASP calculations of bulk Bi_2Se_3 in the conventional three-formula-unit hexagonal cell and for a variety of computational approaches. Corresponding experimental values from three different studies are also reported ([a]Ref. [82], [b]Ref. [83], [c]Ref. [84]). In each column, the values in **bold** (*italics*) are the closest (second closest) values to experimental data from Expt.[c] [84].

	a (Å)	c (Å)	V (Å^3)	Se_2-Bi (Å)	Se_1-Bi (Å)	vdW gap (Å)
Expt.[a]	4.143	28.636	425.670	3.03	2.89	2.568
Expt.[b]	4.138	28.624	424.568	3.04	2.87	2.590
Expt.[c]	4.135	28.615	423.819	3.06	2.86	2.530
PBE	4.190	31.410	477.590	3.10	2.88	3.441
PBE + SOC	4.201	30.663	468.574	3.11	2.89	3.168
PBE + vdW(D2)	*4.125*	28.975	*427.000*	*3.06*	**2.86**	2.664
PBE + vdW(D2) + SOC	**4.135**	**28.713**	**425.064**	**3.06**	*2.87*	**2.555**
PBE + vdW(D3)	4.175	*28.886*	436.127	3.09	2.87	*2.649*
LDA	4.107	27.949	408.372	3.04	2.84	2.385
LDA + SOC	4.116	27.714	406.654	3.04	2.85	2.277
LDA + vdW(D2)	4.057	27.092	386.238	2.99	2.82	2.173
LDA + vdW(D2) + SOC	4.062	26.920	384.667	2.99	2.83	2.084

(DM) [80,81] vector D_{ij}, which can be obtained via the expression $\vec{e}_i{}^T \mathbb{J}_{ij}^A \vec{e}_j = D_{ij} \cdot (\vec{e}_i \times \vec{e}_j)$. In absence of SOC, Eq. (2) reduces to Eq. (1). As for the nonrelativistic mapping, alternative definitions of the parameters entering Eq. (2) are possible [75]. The computational settings for the calculations of the interatomic exchange interaction are similar to those described above, but a larger sampling of the Brillouin zone was needed to have converged values for all distances covered by the plots shown in the next sections. In the conventional three-formula-unit hexagonal cell, a **k** mesh of $70 \times 70 \times 24$ was used. When doubling the unit cell, the **k** mesh was scaled in a way to maintain the desired precision, which allowed for a smaller sampling along the c axis.

III. DETAILS OF THE STRUCTURAL OPTIMIZATION

A. Choosing the best method for pristine Bi_2Se_3

We first search for what computational method is going to provide the best results for pristine Bi_2Se_3, when comparing to the experimental structural data. We shall then use that method for the structural optimization of our doped magnetic systems. We consider various combinations of exchange-correlation functionals, and inclusion of SOC and vdW corrections, as illustrated in detail in Sec. II. The most relevant structural parameters obtained from all our calculations are given in Table I, alongside the corresponding experimental values [82–84]. We observe that GGA-PBE alone overestimates the lattice parameters and bond lengths. The inclusion of the vdW corrections improves the agreement with the experimental values substantially for both in-plane and out-plane degrees of freedom. SOC causes smaller modifications by increasing the in-plane bonds but decreasing the interlayer distance. LDA, on the other hand, underestimates the structural degrees of freedom and the inclusion of SOC further enhances this effect. The DFT-D2 method for vdW corrections that we use is not compatible with the LDA functional, as the functional parametrization is incomplete. Out of curiosity, we applied the vdW correction to the LDA functional by using the GGA-PBE parameter value. The obtained results (see the last two rows in Table I) show a large underestimation of the structural parameters and therefore this approach cannot be used for these systems. The values in bold (italics) in each column are the closest (second closest) values to the most recent experimental values [84] that we obtain from our calculations. We also note that the next generation of vdW correction by Grimme, i.e., D3 [85], does not improve on the results, but leads to too large in-plane distances. Overall, we conclude that PBE with vdW and SOC corrections gives the best result. The next best method is PBE with only vdW corrections. However, the SOC-induced corrections to the structural parameters are not very large, but involve a much larger computational cost. This suggests that the PBE+vdW method may offer the best compromise between accuracy and computational cost for large supercells.

B. Doping Bi_2Se_3 with TM impurities

Most studies of the magnetic coupling so far have provided a model of magnetically doped TIs in the dilute limit, either by using large supercells or the coherent potential approximation (CPA) [27,35,64,86]. In this paper, we are interested in understanding the evolution of the magnetism starting from the full in-plane coverage and gradually going towards the dilute limit. Therefore, we focus on doping a single Bi layer within a single QL in the conventional three-formula-unit hexagonal cell, as shown schematically in Fig. 1(a). For convenience, we label such a layer "the magnetic Bi layer". This name will be used in the rest of the paper to specify the planar concentration of dopants, as shown in Fig. 1(b). Investigated dopants include four TM elements, namely, V, Cr, Mn, and Fe. The other QLs in the system for now remain undoped, with the idea of creating a hypothetical 2D-like magnet inside a layered nonmagnetic TI. The large distance between the TM layers in the supercell quenches the out-of-plane magnetic coupling, and the only finite interatomic exchange interaction remains the intralayer in-plane term ($J_{\text{intra}-\text{in}}$) between the TM atoms in the same Bi layer of the same QL, as shown schematically in Fig. 1(c). The reason for considering a model 2D magnetic system like the present one is that we want

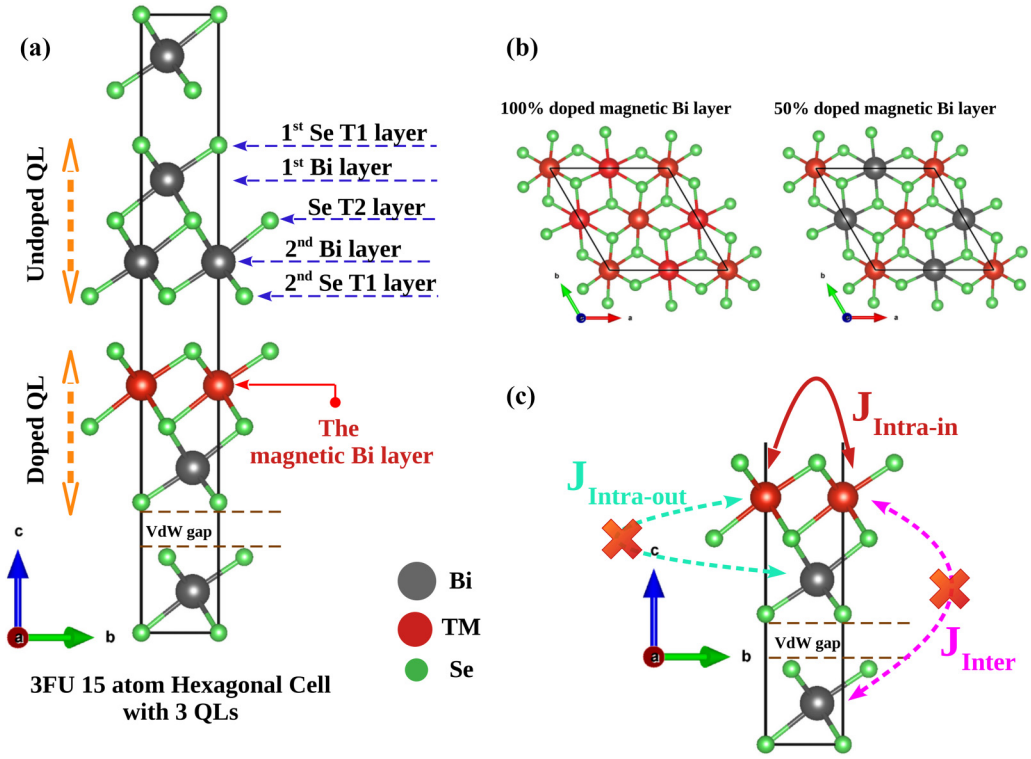

FIG. 1. (a) Conventional three-formula-unit (3FU) hexagonal cell of Bi_2Se_3 where one of the Bi layer inside a QL has been doped with TM atoms and labeled as "the magnetic Bi layer". Different atomic layers and planes in the undoped QLs are also shown. Bi, Se, and TM atoms are indicated by grey, green, and red spheres, respectively. (b) A bird's eye view of the magnetic Bi layer where 100% and 50% of the Bi atoms have been replaced with TM dopants. (c) A sketch of the possible inter-atomic exchange couplings expected in realistic TM-doped Bi_2Se_3, with the assumption that doping happens substitutionally at the cationic site; note that in our model both $J_{\text{intra}-\text{out}}$ and J_{inter} are suppressed. Details given in the main text.

to study the origin and nature of the in-plane magnetic exchange interaction, $J_{\text{intra}-\text{in}}$, between the TM atoms, and their dependence as a function of in-plane doping concentrations in an ideal environment in the absence of the interlayer (J_{inter}) and out-of-plane intralayer ($J_{\text{intra}-\text{out}}$) interactions, also depicted in Fig. 1(c). The $J_{\text{intra}-\text{in}}$ interaction that we consider here is supposed to be the easiest one to model, analyze, and understand, but can incorporate all the possible exchange mechanisms that usually occur in these systems under a more realistic doping. By comparing the detailed understanding of the magnetic interactions in this ideal system and the changes that will appear when different kinds of doping are allowed, we shall be able to understand how the exchange coupling really originates in tetradymite semiconductors. Furthermore, this type of analysis will also allow us to investigate the role of local distortions and structural anisotropy resulting from the doping process directly, connecting them to the nature of the exchange coupling. This analysis cannot be done via a mean-field approach as CPA, but requires the usage of large supercells [87]. As a result, one has to limit the configurations to explore to avoid an explosion of the computational costs.

It is important to note that, in a realistic system, the random distribution of substitutional impurities within the Bi matrix will introduce additional out-of-plane couplings, both inside the same QL ($J_{\text{intra}-\text{out}}$) and between QLs ($J_{\text{inter}}$); see again Fig. 1(c). The inclusion of J_{inter} is not essential for the purpose of analyzing the nature of the exchange mechanism, since this coupling is much weaker than those happening inside the same QL, due to the presence of the wide vdW gap [27]. Similar considerations can be made for interstitial impurities, which may appear in the vdW gap, albeit with a very small concentration [86]. Although the presence of these additional magnetic atoms may induce a small renormalization of the intralayer couplings, it is not expected to change their characteristics and physical origin. A more impactful effect may be expected for the ordering temperature [27,86], which is, however, not the goal of our analysis. Neglecting $J_{\text{intra}-\text{out}}$ is instead a choice dictated by computational convenience, as illustrated above. Based on previous literature [27], we expect this term to be of a similar nature as $J_{\text{intra}-\text{in}}$ and therefore we believe that our analysis may be extended to it as well. We intend to investigate this hypothesis in future works, using the results presented here as a term of comparison.

C. Structural optimization method for TM-doped Bi_2Se_3

For the structural optimizations of the doped systems, the computational approach is decided on the basis of the results obtained for pristine Bi_2Se_3. Thus, we choose GGA-PBE+vdW as the exchange-correlation functional and include SOC for a reliable treatment of the heavy atom Bi. To improve on the deficiencies of semi-local exchange-correlation functionals, a Hubbard U correction is added to the TM-3d states, via the DFT + U approach. Thus, we explore the role of these different corrections in a series of

TABLE II. Calculated lattice constants a and c, cell volume V, nearest-neighbor (NN) cation-anion bond lengths, TM-projected spin moment and total spin moment over the entire cell for Cr-doped Bi_2Se_3, for a concentration of 100% in the magnetic Bi layer. Calculations made with VASP, using different methodological schemes, as described in the text.

				NN bonds in doped QL (Å)					NN bonds in undoped QL (Å)			Moment (μ_B)	
Method	a (Å)	c (Å)	V (Å^3)	Cr-Se_2	Cr-Se_1	Bi-Se_2	Bi-Se_1	vdW gap	Bi-Se_2	Bi-Se_1	vdW gap	TM	cell
PBE + vdW	4.05	28.53	405.32	2.68	2.61	3.09	2.83	2.73	3.05	2.84	2.72	3.23	3.00
PBE + vdW + U	4.06	28.57	407.79	2.71	2.64	3.09	2.83	2.71	3.06	2.84	2.71	3.52	3.00
PBE + vdW + SOC	4.06	28.35	403.87	2.68	2.61	3.11	2.83	2.67	3.06	2.85	2.62	3.23 $\hat{\mathbf{z}}$	3.00 $\hat{\mathbf{z}}$
PBE + vdW + SOC + U	4.07	28.37	406.28	2.71	2.64	3.11	2.84	2.66	3.06	2.85	2.61	3.52 $\hat{\mathbf{z}}$	3.00 $\hat{\mathbf{z}}$

calculations, performed by replacing an entire Bi layer inside a QL with TM impurities, as illustrated in Fig. 1(a). This means that we have 100% doping in reference to the magnetic Bi layer, 50% doping in reference to the QL, a 17% doping in reference to the conventional three-formula-unit hexagonal unit cell used for the calculations. The differences obtained between the various computational methods do not depend on the choice of the TM impurity, thus it is sufficient to look only at the results for one element. The structural data as well as the most relevant magnetic moments obtained for Cr-doped Bi_2Se_3 are reported in Table II. By first comparing PBE+vdW and PBE+vdW+U, we see that the effect of U is to increase the local Cr-Se bonds by about 0.03 Å, without affecting the Bi-Se bonds in both the doped and undoped QLs. The correction induced by U also causes an increase of the lattice parameters, leading to a slightly larger equilibrium volume. This is due to having decreased the itinerant character of the Cr-3d states and thus their participation to the chemical bond [46]. Conversely, the inclusion of SOC does not affect the Cr-Se bonds significantly. Relativistic corrections slightly increase the Bi-Se bonds and reduce the cell volume, albeit less than 0.5%. We also notice that the structural changes induced by U and SOC seem to compensate each other. As a result, the final structural data obtained for PBE+vdW+U+SOC are very similar to those obtained with PBE+vdW, which, however, involves a much smaller computational cost. In addition, the small structural changes observed in Table II have a negligible effect on the electronic structure. This can be verified by employing the four equilibrium equilibrium structure to calculate the electronic structure while keeping the computational scheme fixed. As illustrated in the SM [71], the structural variations have a negligible effect on the electronic structure. Overall, we can conclude that the major structural changes resulting from doping are well captured within the PBE+vdW approach. Therefore, we are going to use this approach to obtain all the relaxed structures investigated in the rest of this paper, encompassing different dopant concentrations and magnetic orders. The effect of U and SOC on the electronic and magnetic properties will be instead analyzed directly in the RSPt calculations. The only comment to be made in reference to Table II is that SOC does not induce any substantial variation on the calculated spin moment.

IV. FULL COVERAGE (100% DOPING) OF THE MAGNETIC BI LAYER

The structural changes resulting from the TM doping as obtained from the VASP calculations are reported in Table III. The most visible effect of doping is the decrease in the lattice parameters and unit cell volume, as a result of the smaller size of the TM atoms compared to Bi. As emphasized in previous literature [27,32,88], the local relaxation is particularly important for the magnetic properties. The TM-Se bonds are much smaller than the Bi-Se bonds, accounting for the difference in the atomic radii. As expected, the Bi-Se bonds in the undoped QLs remain unaffected by the doping and maintain their pristine chemical properties. Going from V to Fe, the TM-Se bonds do not show any systematic change with the atomic number, which highlights the role played by the magnetic degrees of freedom, in addition to the atomic size. A parameter which is instead clearly connected to the atomic number is the size of the vdW gap between the QL doped with TM atoms and an adjacent QL, which systematically decreases from V (2.83 Å) to Fe (2.59 Å). As a result, the electronic and magnetic properties of the Mn- and especially Fe-doped layers are expected to be more affected by the neighboring undoped QLs compared to V- and Cr-doped layers. The distance between two undoped QLs, instead, is constant for V, Cr, and Mn, but shows a small variation for Fe, which is also noticeable in the total equilibrium volume.

TABLE III. Calculated lattice constants a and c, cell volume V, and NN cation-anion bond lengths for TM-doped Bi_2Se_3, for a concentration of 100% in the magnetic Bi layer, as obtained with VASP in PBE + vdW.

				NN bonds in doped QL (Å)					NN bonds in undoped QL (Å)		
TM atom	a (Å)	c (Å)	V (Å^3)	TM-Se_2	TM-Se_1	Bi-Se_2	Bi-Se_1	vdW gap	Bi-Se_2	Bi-Se_1	vdW gap
V	4.06	28.59	407.42	2.77	2.54	3.08	2.83	2.83	3.05	2.84	2.72
Cr	4.05	28.53	405.32	2.68	2.61	3.09	2.83	2.73	3.05	2.84	2.72
Mn	4.06	28.55	406.87	2.75	2.59	3.09	2.84	2.67	3.05	2.84	2.72
Fe	4.05	28.29	401.06	2.77	2.55	3.04	2.84	2.59	3.04	2.84	2.67

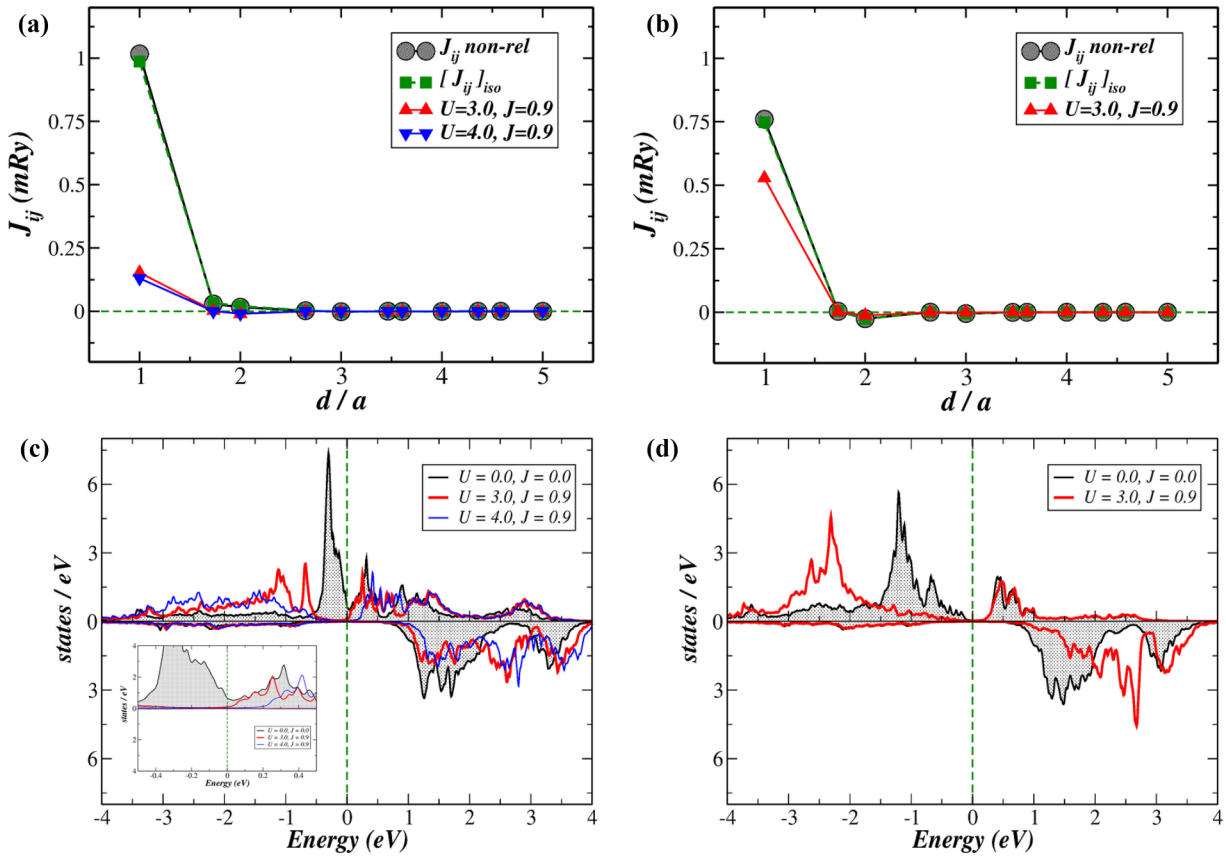

FIG. 2. (a) Interatomic exchange interactions between magnetic moments at the V sites in V-doped Bi_2Se_3 for 100% doping of the magnetic Bi layer as a function of the V-V distance. Calculations made with RSPt in DFT and DFT + U, without and with SOC. For the latter, only the isotropic averages of the exchange tensor are plotted (green squares). (b) Interatomic exchange interactions between magnetic moments at the Cr sites in Cr-doped Bi_2Se_3 for 100% doping of the magnetic Bi layer, as a function of the Cr-Cr distance. Calculations made with RSPt in DFT and DFT + U, without and with SOC. For the latter, only the isotropic averages of the exchange tensor are plotted (green squares). (c) Spin-polarized PDOS of the V-3d states in DFT and DFT + U, as calculated via RSPt, with the Fermi level at zero energy; in the inset, the states at the Fermi level are magnified, showing a finite contribution for plain DFT but not for DFT + U. (d) Spin-polarized PDOS of the Cr-3d states in DFT and DFT + U, as calculated via RSPt, with the Fermi level at zero energy.

The relaxed structures are used in RSPt to determine electronic and magnetic properties. Let us first focus on V- and Cr-doped Bi_2Se_3. The interatomic exchange parameters calculated for V and Cr are shown in Figs. 2(a) and 2(b), respectively. We can see that the isotropic values calculated without SOC (black spheres) are identical to the isotropic averages calculated with SOC (green squares). For these elements, relativistic corrections do not change the nature of the magnetic exchange interaction, not even quantitatively. This is somehow expected for 100% doping of the magnetic Bi layer, since the heavy Bi atoms inside this layer are all replaced by TM atoms and thus are not present along the exchange paths. This is in agreement with previous studies where heavy Cr doping in (Bi, Sb)$_2$Se$_3$ was found to turn the system into a FM insulator where the effects due to SOC are strongly quenched [89,90]. The dependence of the calculated exchange parameters on the interatomic distances is found to be short-ranged, for both V and Cr. The nearest-neighbor (NN) interaction is the largest and has a ferromagnetic character [positive sign, due to the convention adopted in Eqs. (1) and (2)]. The second- and third-neighbor interactions are already very small in comparison to the NN coupling, and therefore we conclude that, in this case, only the NN term is going to play a significant role in the magnetic ordering. To gain a precise understanding of the nature and origin of the NN interaction, we take advantage of the octahedral symmetry and extract the orbital resolved $E_g - E_g$, $T_{2g} - T_{2g}$, and $E_g - T_{2g}$ components of the NN exchange interaction, which are presented in Table IV. Additionally, the table includes the projected local charges for the TM-3d states (Q_d) for different spin channels, their differences (ΔQ) corresponding to the TM-3d moment, and the total local moment at the TM site (μ_{TM}). Let us first look at the data for the V-doped system, without the correction of the Hubbard U. Table IV shows that a magnetic moment of almost 2 μ_B forms at each V site; these magnetic moments are coupled by a strong FM NN interaction, whose major contributions come from the $T_{2g} - T_{2g}$ component (0.67 mRy) and, to a lesser extent, the $E_g - T_{2g}$ component (0.37 mRy). In past studies of the dilute limit, a local magnetic moment of about 2 μ_B was suggested to be the signature of a d^2 electron configuration in the 3+ oxidation state [27,32,64]. However, this interpretation is based on the assumption of an atomic-like scenario where Hund's rules apply, which is doubtful for this class

TABLE IV. Orbital-resolved NN exchange parameters, spin-resolved TM-3d charges (Q_d) and their differences (ΔQ), and total magnetic moment at the TM site (μ_{TM}) for TM-doped Bi_2Se_3 for 100% doping of the magnetic Bi layer, as obtained with RSPt in DFT and DFT + U without SOC.

		Orbital-resolved NN exchange parameters (mRy)				Spin resolved d-orbital charge (electron unit)			
TM atom	U, J (eV)	E_g–E_g	T_{2g}–T_{2g}	E_g–T_{2g}	Total	Q_d-up	Q_d-dn	ΔQ	μ_{TM} (μ_B)
V	0.0, 0.0	−0.024	0.670	0.371	1.017	2.38	0.45	1.93	1.96
	3.0, 0.9	−0.073	−0.064	0.291	0.153	2.32	0.44	1.88	1.91
	4.0, 0.9	−0.059	−0.056	0.246	0.130	2.32	0.42	1.90	1.93
Cr	0.0, 0.0	0.000	−0.076	0.836	0.760	3.42	0.45	2.97	3.03
	3.0, 0.9	−0.013	−0.017	0.557	0.528	3.45	0.40	3.05	3.10
Mn	0.0, 0.0	0.391	−0.100	−0.271	0.019	4.28	0.58	3.70	3.77
	3.0, 0.9	0.359	−0.011	0.004	0.353	4.42	0.42	4.00	4.07
Fe	0.0, 0.0	1.505	0.777	−5.115	−2.832	4.41	1.53	2.88	2.92
	3.0, 0.9	0.004	−1.220	−0.448	−1.665	4.61	1.27	3.34	3.39

of systems. A detailed analysis of XMCD experiments on V-doped $(Bi, Sb)_2Te_3$, based on multiplet ligand field theory calculations, suggests that the 3+ configuration contributes to less than 10% to the ground state, while the most important contributions come from the configurations with one and two ligand holes [26,35]. This is also supported by the analysis of the local density matrix in DFT, which points to a nominal oxidation state around 2+, as a consequence of a strong $p-d$ hybridization [35]. The latter leads to a redistribution of electronic charge along the covalent bond between V and Te (Se in our case), thus impeding its contribution to the free carrier concentration [26]. This scenario finds correspondence in our model, despite being for the full coverage of a Bi layer and not in the dilute limit. In fact, the TM-3d charge reported in Table IV is very close to a d^3 configuration, with partial occupation of both spin-up and spin-down bands. This can be visualized in the projected density of states (PDOS) for the V-3d states, reported in Fig. 2(c) as a grey-shaded region. Due to the presence of a small charge in the minority spin channel, partially filled T_{2g}-up states appear as an impurity band in the majority spin channel, with a finite contribution at the Fermi level (E_F). The empty E_g-up states are further higher in energy in the conduction band. In this situation, a virtual hopping from the partially filled T_{2g}-up states to the empty E_g-up states of the NN V atoms is possible through the Se atoms. A nearly 90° angle in this V-Se-V exchange channel can give rise to an FM superexchange following the Goodenough-Kanamori-Anderson (GKA) rules [91]. A similar mechanism has indeed been described in VI_3 for a localized moment of about 2 μ_B, albeit in a d^2 configuration [65]. The virtual hopping process mentioned above involves two component mechanisms. First, a spin parallel electron is transferred from the filled p-orbital of the Se atom to the empty E_g-up orbital of the first V atom. This results in an energy gain following intra-atomic Hund's rule and leading to an FM V-Se coupling. The second electron from the Se p-orbital couples antiferromagnetically with the filled T_{2g} orbital of the second V atom, due to a direct exchange between nonorthogonal orbitals. The net $E_g - T_{2g}$ exchange between the two V atoms becomes FM. This analysis suggests that the FM $E_g - T_{2g}$ component comes from a superexchange mechanism. Moreover, a virtual hopping between the partially filled T_{2g}-up orbitals of two NN V atoms is also possible. This can result in a $T_{2g} - T_{2g}$ FM superexchange mechanism, which again has been discussed in the context of VI_3 [65]. This contribution may be substantial, but cannot overweigh the $E_g - T_{2g}$ FM superexchange, as the latter involves a sigma bonding between the Se p-orbital and the V E_g-orbital along the bonding axis [91]. Finally, we already commented on the presence of a finite spectral weight at E_F, due the T_{2g}-up states, which is also magnified in the inset of Fig. 2(c), for clarity. These states may cause the $T_{2g} - T_{2g}$ FM double-exchange mechanism [38,92], which can be quite large and hence dominate over the superexchange interactions. In order to understand if double exchange is really the mechanism driving the large $T_{2g} - T_{2g}$ coupling seen in Table IV, we investigate the connection between this term and the number of states at E_F. To modify the latter, we perform DFT + U calculations with interaction parameters $U = 3.0$ eV and $J = 0.9$ eV. The precise values of the Coulomb interaction parameters are not important for this test, since we intend only to analyze the response of the system to a depletion of states at E_F. The exchange parameters (red up-triangles) and orbital projected 3d-states (red lines) obtained from these calculations are shown in Figs. 2(a) and 2(c), respectively. As expected, introducing the additional U term drives the system insulating, opening a gap at the Fermi level in the spin-up channel. As a result, the interatomic exchange interactions show a noticeable change in the NN $T_{2g} - T_{2g}$ component, which goes from being the dominant FM term (0.67 mRy) to being a very weak AFM term (−0.06 mRy). The latter corresponds to what is expected from an interaction coming from the superexchange in an insulating state [91]. This analysis confirms that the dominant NN $T_{2g} - T_{2g}$ component observed without U comes from a double-exchange mechanism. Our conclusion is also supported by results obtained from multiplet ligand field theory, where the ground state is decomposed in an almost equal admixture of d^3 and d^4 configurations [26]. We also note that in DFT + U the $E_g - T_{2g}$ FM superexchange becomes the dominant exchange mechanism, but its value is decreased from 0.37 mRy (no U case) to 0.29 mRy. This is due to the increased energy separation between the filled and empty bands in the spin-up channel; see Fig. 2(c). To further explore whether the FM superexchange mechanism remains prevalent,

we also increase U to 4 eV. These calculations reveal a further increase in the aforementioned separation between filled and empty bands in the spin-up channel; see the blue curves in Fig. 2(c). This results in a further decrease of the strength of the FM superexchange $T_{2g} - E_g$ component, which goes from from 0.29 mRy to 0.25 mRy (Table IV).

As we go from V to Cr, one more electron is added to the d-orbital. Consequently, we can anticipate a d^4 electron configuration if Cr is in a 2+ oxidation state analogous to the one we discussed for V (see the final remarks in the conclusions for a contextualization of this analysis). This is confirmed by the analysis of Table IV, where the Cr-3d states have a total occupation of about 3.9 electrons and a spin moment of almost 3 μ_B. The local and total magnetic moments are in line with previous DFT findings for similar Cr-doped systems [27,64]. Multiplet ligand field theory and XMCD analysis of Cr-doped $(Bi, Sb)_2Te_3$ point to a ground state composed by d^3 (10%), d^4 (50%), d^5 (35%), and d^6 (4%) configurations, which is also consistent with our data [26]. In the PDOS for the Cr-3d orbitals shown in Fig. 2(d), we observe a filled valence band of mainly T_{2g}-up states and an empty conduction band of mainly E_g-up character. A large separation between valence and conduction bands creates an insulating gap. Unlike the V-doped system, this insulating gap eliminates the possibility of a $T_{2g} - T_{2g}$ FM double exchange mechanism. The component analysis of the NN exchange, provided in Table IV, supports this conclusion, showing a weak AFM $T_{2g} - T_{2g}$ component. This can again be rationalized by following the GKA rules [91], as described above. In this case, the virtual hopping between filled T_{2g}-up states and vacant E_g-up states gives rise to the dominant $E_g - T_{2g}$ FM superexchange of 0.84 mRy. These observations can be connected to the analogous system CrI_3, where Cr exhibits a magnetic moment of about 3 μ_B and a nearly 90° Cr-I-Cr exchange path, albeit in a 3+ oxidation state [93,94]. Following what was done for the V case, we can again make DFT + U calculations with $U = 3.0$ eV and $J = 0.9$ eV for the Cr-3d states and observe the system response. The calculated exchange parameters (red triangles) are plotted in Fig. 2(b), while the corresponding PDOS for the Cr-3d states (red bold lines) is plotted in Fig. 2(d). The corrections induced by the local Coulomb interaction increase the separation between occupied and empty states, leading to an increased band gap. The latter results in a decrease in the NN $E_g - T_{2g}$ superexchange interaction from 0.84 mRy to 0.56 mRy, similarly to what happens for V. This term, however, remains the dominant contribution to the NN exchange. Interestingly, the AFM NN $T_{2g} - T_{2g}$ superexchange interaction decreases slightly when U is applied (see Table IV). The exchange coupling being finite only at small distances, the long-range behavior of distant neighbors seems to remain unaffected when going from DFT to DFT + U; see Fig. 2(b).

These results show that for V, both double exchange and superexchange could result in a short-ranged FM interaction due to a partially filled T_{2g} band, where the double exchange mechanism strongly depends on the states around the Fermi energy. For Cr, however, there are no states at the Fermi level, and thus only the superexchange mechanism is possible. Our results are in agreement with a recent study [35] where the dependence of the calculated exchange parameter on the position of the Fermi energy is found to be different in V- and Cr-doped Sb_2Te_3. They show that for V, a sharp peak followed by a broad ridge appears in $J_{ij}(E)$ when E_F moves from inside the V T_{2g} manifold to in between T_{2g} and E_g. The sharp peak has been associated with a double exchange mechanism that does not appear for the Cr system. The broad ridge has been associated with a superexchange mechanism which is present in both V and Cr systems.

The electronic and magnetic properties of Mn- and Fe-doped systems are slightly different from those of V- and Cr-doped systems. Table IV shows that Mn-3d states acquire a charge of 4.28 and 0.58 electrons in the spin-up and spin-down channels, respectively. This results in a net 3d moment of about 3.70 μ_B, which is reinforced by a contribution of 0.07 μ_B coming from the other shells of the Mn atom. Overall, this suggests a d^5 electron configuration with Mn in the 2+ oxidation state similar to what was obtained for V and Cr. This interpretation is supported by the PDOS of the Mn-3d states, shown in Fig. 3(c) (black lines). The major contribution to the spin-up channel is located well below the Fermi energy, in the energy window comprised between −5 and −1 eV. A smaller contribution to the spin-up channel is present at the Fermi energy, as a shoulder between a small occupied peak and a small unoccupied peak. The total DOS, which is also shown in Fig. 3(c) (shaded area), clarifies that this spectral weight is due to a localized electron-hole pair, whose major contribution comes from the host. As illustrated in the inset of Fig. 3(c), the Se-4p states (green lines) seem to play a key role. This suggests the presence of a hole on the Se atoms near the Mn atom and the hybridization with the Mn E_g states gives it some E_g character. This finding aligns with experimental studies of Mn-doped Bi_2Se_3, where XAS measurements demonstrate that Mn favors a 2+ oxidation state and acts as a p-type carrier system due to the presence of a ligand hole [95]. Similar conclusions were reached by other theoretical studies on analogous systems [64,96]. As a matter of fact, this physical situation is reminiscent of the behavior of substitutional Mn atoms in Mn-doped GaAs [97–101]. The contribution of the Mn-3d orbitals with E_g character to the hole state comes from the $p - d$ hybridization suggesting a possible hopping of the hole from Se to neighboring Mn atoms. This can lead to a hole-mediated exchange between the Mn atoms, which may manifest as a Zener $p - d$ exchange mechanism or as a particular type of double-exchange, depending on the localization of the aforementioned holes [38–40,99]. To better understand the nature of the exchange coupling, we again focus on the symmetry-resolved components of the NN interaction, as presented in Table IV. Mn with a d^5 electron configuration in the high spin state suppresses the $E_g - T_{2g}$ FM superexchange. Now we get a weak $E_g - T_{2g}$ AFM superexchange for the nearly 90° Mn-Se-Mn exchange path according to GKA rules. This is very similar to what we see in compounds like $MnCl_2$, and $MnBr_2$ having a similar exchange path and Mn^{2+} ion [91]. A small AFM $T_{2g} - T_{2g}$ superexchange is also present, in analogy to what is seen for V and Cr. The $E_g - E_g$ interaction now becomes FM, with an interaction strength comparable to the AFM $E_g - T_{2g}$ superexchange. This competition between FM and AFM components results in a negligible NN exchange coupling, which is even surpassed by the second-neighbor term, as shown in Fig. 3(a). At first one may expect that the FM $E_g - E_g$ interaction may

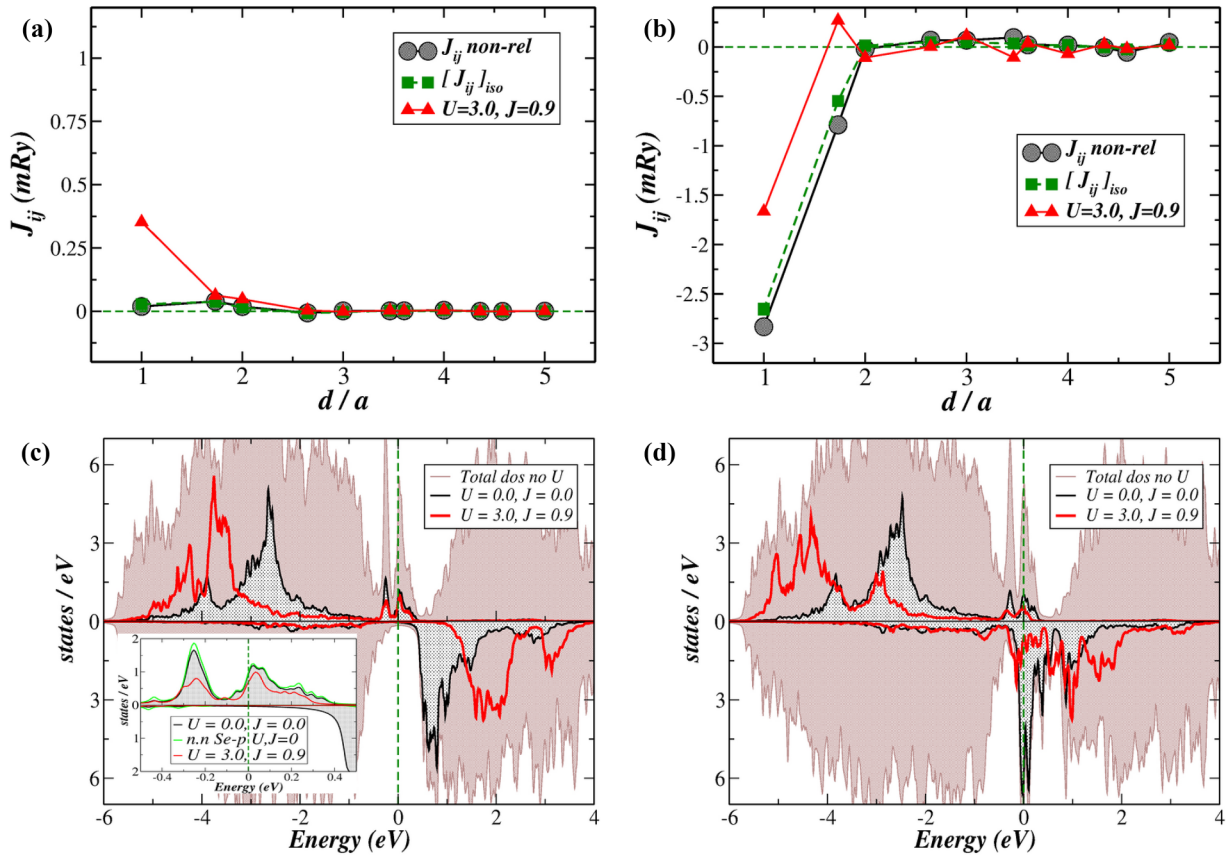

FIG. 3. (a) Interatomic exchange interactions between magnetic moments at the Mn sites in Mn-doped Bi_2Se_3 for 100% doping of the magnetic Bi layer, as a function of the Mn-Mn distance. Calculations made with RSPt in DFT and DFT + U, without and with SOC. For the latter, only the isotropic averages of the exchange tensor are plotted (green squares). (b) Interatomic exchange interactions between magnetic moments at the Fe sites in Fe-doped Bi_2Se_3 for 100% doping of the magnetic Bi layer, as a function of the Fe-Fe distance. Calculations made with RSPt in DFT and DFT + U, without and with SOC. For the latter, only the isotropic averages of the exchange tensor are plotted (green squares). (c) Spin-polarized total DOS and PDOS of the Mn-3d states in DFT and DFT + U, as calculated via RSPt, with the Fermi level at zero energy; in the inset, the states at the Fermi level are magnified, showing a strong hybridization between Mn-3d and Se-4p states. (d) Spin-polarized total DOS and PDOS of the Fe-3d states in DFT and DFT + U, as calculated via RSPt, with the Fermi level at zero energy.

arise from the superexchange mechanism, due to the d^5 electron configuration [91]. However, such a term would be much weaker than what results from our calculations and ignores the complexity of the hole-mediated exchange coupling that we discussed above. Depending on the properties of the hole, two types of hole-mediated exchange can occur as explained in the Mn-doped Bi_2Te_3 theoretical findings [96]. A weakly bound hole leads to an RKKY-type long-range interaction, whereas a strongly bound hole is expected to result in a FM double exchange mechanism. To understand the nature of the $E_g - E_g$ component, we again perform DFT + U calculations, in analogy to the V and Cr cases. Our aim is to perturb the hole state around the Fermi energy and register the eventual changes of the exchange interaction. Surprisingly, we find that the $e - h$ bound state near the Fermi level hardly gets affected by a Hubbard term applied to the Mn-3d states, as illustrated by the red lines in Fig. 3(c). This confirms our previous claim that this state possesses a dominant Se p-character. As a result, the hole-mediated FM $E_g - E_g$ interaction also remains unaffected; see Table IV. Conversely, the AFM $E_g - T_{2g}$ and $T_{2g} - T_{2g}$ superexchange interactions are drastically quenched, which is due to the increased exchange splitting shown by the red lines in Fig. 3(c). Consequently, the total NN exchange interaction J_{ij} is not null any longer but is dominated by the FM $E_g - E_g$ component. The spatial dependence of J_{ij}, as illustrated by the red lines in Fig. 3(a), exhibits a rapidly decaying FM behavior and not an oscillatory trend. This indicates that in our case the $E_g - E_g$ component comes from a short-range double exchange mechanism due to the strongly bound nature of the hole. This is expected in the case of Bi_2Se_3 as a host, which supports more localized properties in comparison to Bi_2Te_3, due to the smaller size of the Se p orbitals [33,96]. Finally, we analyze the effect of SOC on the exchange coupling of Mn dopants; see the green curve in Fig. 3(a). As for V and Cr, there are no noticeable differences arising from relativistic corrections.

Going from Mn to Fe adds one more d electron in the system. The electronic charges reported in Table IV suggest a d^6 configuration and thus a nominal oxidation state of 2+. The corresponding PDOS of the Fe-3d states are shown by the black lines in Fig. 3(d). The structure of the spin-up channel is very similar to the Mn case, with the presence of an

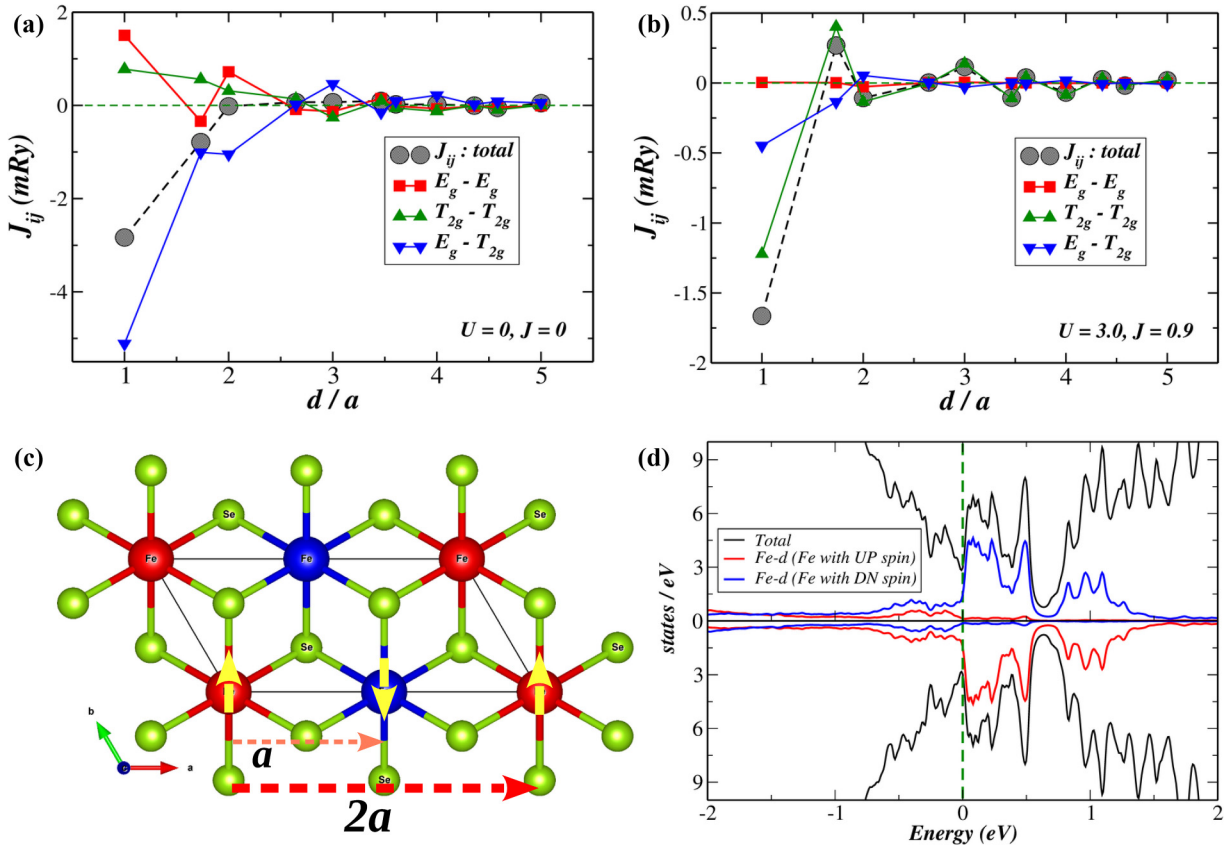

FIG. 4. (a) Orbital decomposition of the interatomic exchange interactions between magnetic moments at the Fe sites in Fe-doped Bi_2Se_3 for 100% doping of the magnetic Bi layer as a function of the Fe-Fe distance. Calculations made with RSPt in DFT without SOC. (b) As above for calculations made with RSPt in DFT + U without SOC, for $U = 3.0$ eV and $J = 0.9$ eV. (c) A simple model where FM chains of Fe atoms are antiferromagnetically aligned, resulting in a unit cell doubling along the a axis. Red and blue spheres represent Fe atoms with magnetic moments up and down, respectively, as also indicated by the yellow arrows. Green spheres represent Se atoms. (d) Spin-polarized total DOS and PDOS of the Fe-3d states in DFT for the AFM state depicted in (c), as calculated via RSPt; the Fermi level is at zero energy.

electron-hole state around the Fermi energy. However, in the case of Fe, the peaks are broader and there is a larger contribution (a small peak) precisely at the Fermi level, suggesting a larger delocalization. This is most likely a consequence of the smaller size of the Fe atoms and the stronger $p - d$ hybridization with the Se atoms. The role of the latter can be further analyzed through the inspection of the hybridization function, obtained by means of a mapping onto a single impurity Anderson model [102]. As illustrated in the SM [71], no marked differences can be seen for the hybridization of the Mn-3d and Fe-3d states for the spin-up channel around E_F, which suggests the predominant role of the steric effects. Conversely, the spin-down channel exhibits a much stronger hybridization for Fe than for Mn, starting precisely at the Fermi level. This is reflected in the corresponding PDOS of Fig. 3(d), where a finite contribution at the Fermi level is noticeable, with a dominant Fe-3d character just below E_F and a more mixed character just above E_F. These features of the electronic structure drastically change the nature of the magnetic exchange interaction with respect to the Mn case. As shown in Fig. 3(b) (black spheres), we now get a strong AFM NN exchange, followed by an AFM second-neighbor exchange of significant strength. Both the sign and strength of the exchange interactions are qualitatively very different than those observed in the previous three systems with V, Cr, and Mn. These AFM interactions were also found in a previous DFT-based study of Fe-doped Bi_2Se_3, Bi_2Te_3, and Sb_2Te_3 [27]. Besides this, we also see a distant oscillatory behavior which becomes more prominent in the case of DFT + U calculations, as shown by the red lines in Fig. 3(b). These oscillations are a characteristic signature of the RKKY-type exchange mechanism. Before analyzing the details of the exchange coupling, it is worthwhile to point out that, for Fe, SOC seems to have a larger impact on short-range interactions in comparison to the other systems. Since we are still considering a system where doping amounts to 100% of the magnetic Bi layer, we attribute this effect to secondary factors, as, e.g., induced by local structural distortions. A better analysis of these small corrections requires further investigation, but falls outside the scope of this paper.

To understand the origin of the marked AFM coupling observed in Fe-doped Bi_2Se_3, we again focus on the orbital resolved components of the NN exchange, reported in Table IV. For further insight, we also look at the decomposition of the distance dependence of the exchange coupling, presented in Fig. 4. As for Mn, the $E_g - E_g$ component gives a hole-mediated FM NN exchange, although its strength is significantly bigger for Fe. This component shows a long-

ranged RKKY-type oscillatory trend, as shown in Fig. 4(a) (red squares), which suggests a weakly bound hole similar to what was suggested in the case of Mn-doped Bi_2Te_3 [96]. As discussed above, this weakly bound hole is more delocalized and may result in both short-range FM double exchange or long-ranged RKKY-type exchange. Due to the more delocalized nature of the hole, the NN $E_g - E_g$ component becomes much larger than the one observed for Mn doping. Next, we focus on the $T_{2g} - T_{2g}$ component, depicted as green up-triangles in Fig. 4(a). The initial NN FM interaction gradually decays with distance, followed by a weak oscillatory behavior. The short-ranged FM interactions occur as a result of a double exchange mechanism, due to the finite contribution at the Fermi level coming from the singly occupied T_{2g}-dn states; see Fig. 3(d). The double exchange dominates over the RKKY interaction, due to the strongly localized impuritylike nature of this state. Finally, we discuss the $E_g - T_{2g}$ component (blue dn-triangles) that constitutes the dominating AFM interaction between two Fe atoms. The total DOS, shown in Fig. 3(d), has a large contribution at the Fermi energy in both the spin-up and spin-down channels. The states in the spin-up channel are holelike states with a significant E_g character, as discussed before. On the other hand, the states in the spin-down channel are electrons coming from the partially filled T_{2g}-dn band. Their narrow bandwidth suggests that both these states are localized in nature. Now, an AFM order between two Fe atoms will make it possible for the holes and electrons to hop from the majority spin channel of one Fe to the minority spin channel of the other Fe atom and vice versa. This hopping will happen via the Se atoms and will lead to a hybridization between two different spin channels. This will make the system more metallic with more delocalized charge carriers, promoting a kinetic energy gain. This situation resembles the AFM double-exchange mechanism, that becomes possible in this system because of the 2+ oxidation state of the Fe atom and a d^6 electron configuration.

To check if the previous considerations are correct, we perform an electronic structure calculation where the magnetic order is assumed to be FM along chains of Fe atoms, but AFM between chains, as depicted schematically in Fig. 4(c). Note that the Fe atoms in the plane form a triangular lattice and establishing a different type of AFM order may be much more complicated, involving also noncollinear magnetic moments and complex magnetic textures [103]. Nevertheless, the model devised here is sufficient for our analysis. The total DOS and PDOS of the Fe-3d states for this model AFM calculation are shown in Fig. 4(d). Energetically, this solution is more favorable than the FM solution we discussed above. As by our hypothesis, we get a fully metallic solution with a more delocalized state around the Fermi energy if compared to the FM solution; see Fig. 3(d).

To further verify that our interpretation of the various exchange mechanisms present in Fe-doped Bi_2Se_3 is correct, we have again performed DFT + U calculations to manipulate the electronic structure and observe the induced changes in the exchange interaction. The distance dependence of the exchange components in DFT + U is illustrated in Fig. 4(b), while the PDOS of the Fe-3d states is shown in red in Fig. 3(d). Due to the local Coulomb interaction, the exchange splitting of the Fe-3d states increases and the spectral weight of the holelike state at the Fermi level almost disappears. Qualitatively, this is very different than what observed for Mn, and it is due to the larger $p - d$ hybridization and more 3d character of the hole state compared to the Mn case. In DFT + U, the vanishing hole state is no longer able to give rise to the hole-mediated double exchange and, as a result, the $E_g - E_g$ component of the exchange interaction totally dissipates; see Fig. 4(b). The T_{2g} states in the spin-down channel are also strongly affected by the Hubbard U, with a marked increase of the bandwidth and a reduced contribution at the Fermi level. A reduced contribution at the Fermi level from both the E_g-like hole state in the spin-up channel and the T_{2g} state in the spin-down channel reduces the strength of the AFM double exchange type $E_g - T_{2g}$ component, which is no longer the largest source of the AFM NN exchange. Now, the major contribution comes from the $T_{2g} - T_{2g}$ component, that also shows a prominent long-ranged oscillatory behavior. Though the $T_{2g} - T_{2g}$ shows an NN AFM exchange, the second-neighbor exchange is FM, suggesting a dominating RKKY mechanism. This happens because the DFT + U corrections have slightly increased the delocalization of the T_{2g} states, in connection to the aforementioned increase of bandwidth. The $T_{2g} - T_{2g}$ component also defines the net exchange of the system, with evident long-ranged RKKY behavior. Interestingly, a very similar trend of the $T_{2g} - T_{2g}$ component was reported in the bulk bcc-Fe [47]. These results suggest that in Fe-doped Bi_2Se_3 there are competing exchange interactions that can be tuned to induce various magnetic orders in the system, through the application of local perturbations. Though the high concentration of dopants modeled here depicts a scenario that does not seem suitable for QAHE, due to the AFM ground state, the presence of a prominent RKKY-type interaction suggests that a FM order may be stabilized at lower concentrations and/or via external stimuli. Further investigations are needed to clarify this point. Some insight may be obtained through the analysis of 50% doping of the magnetic Bi layer, which is presented in the next section.

V. HALF COVERAGE (50% DOPING) OF THE MAGNETIC BI LAYER

The previous section has clarified the competition and cooperation of various exchange mechanisms in the magnetic order of TM-doped Bi_2Se_3, in the special limit of the full coverage of a Bi plane in an almost isolated QL, which we defined as the magnetic Bi layer. In this section, we analyze the role played by the dopant concentration, with a main focus on the local structural arrangements of the TM atoms. To this end, we consider a model where the half of Bi atoms in the magnetic Bi layer are replaced by TM atoms, as shown schematically in Fig. 1(b). Ignoring disorder is not important for our analysis, since we are interested in the details of the local response and not in the reproduction of a particular material. For 50% doping of the magnetic Bi layer, the average TM-TM distance obviously increases with respect to the 100% doping case, due to the larger size of the Bi atoms. Most importantly, the exchange paths may be altered by the different distribution of dopants, as schematically illustrated in the inset of Fig. 5(a). The NN exchange path (TM-Se-TM / E_1) for 50% doping of the magnetic Bi layer remains

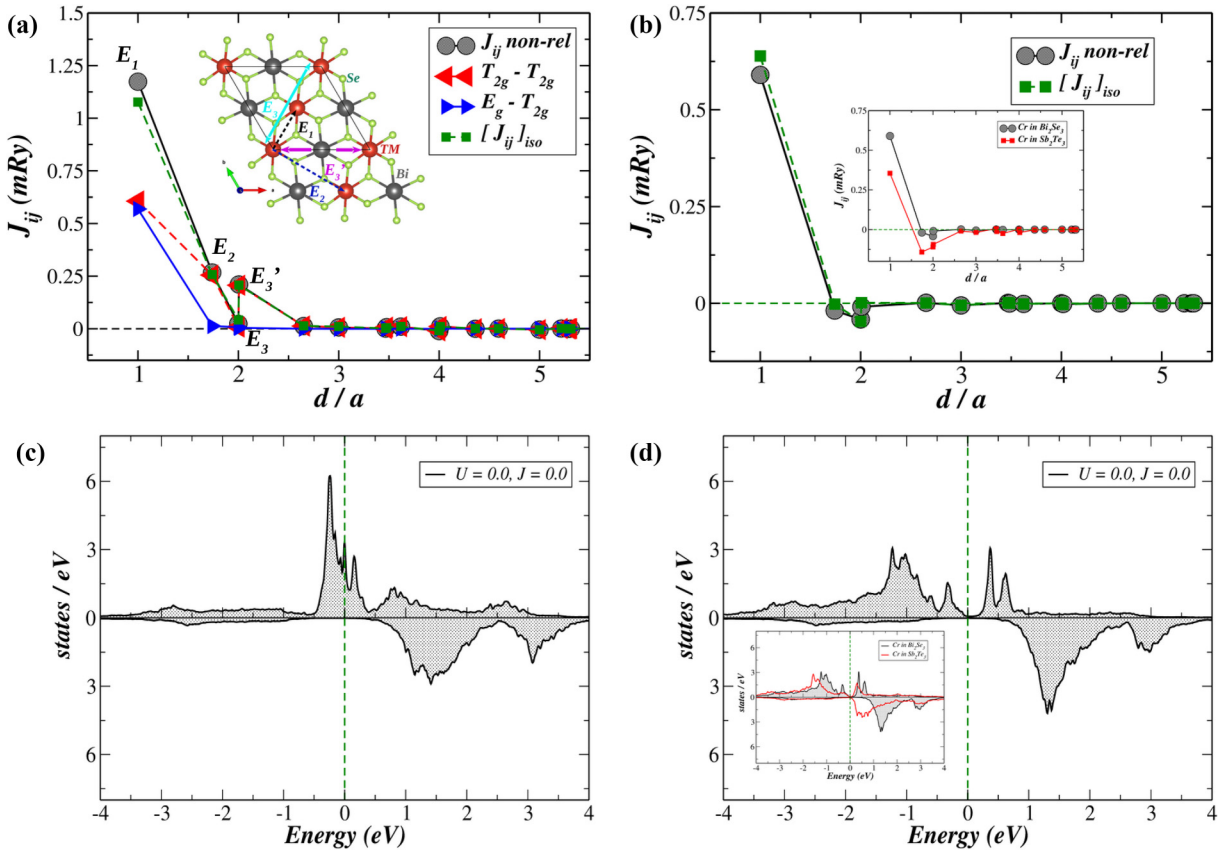

FIG. 5. (a) Orbital-resolved inter-atomic exchange interactions between magnetic moments at the V sites in V-doped Bi_2Se_3 for 50% doping of the magnetic Bi layer, as a function of the V-V distance. Calculations made with RSPt in DFT, without and with SOC. For the latter, only the total isotropic averages of the exchange tensor are plotted (green squares). In the inset, the most relevant exchange paths are shown, as discussed in the main text. (b) Interatomic exchange interactions between magnetic moments at the Cr sites in Cr-doped Bi_2Se_3 for 50% doping of the magnetic Bi layer as a function of the Cr-Cr distance. Calculations made with RSPt in DFT, without and with SOC. For the latter, only the isotropic averages of the exchange tensor are plotted (green squares). In the inset, a comparison is made between the nonrelativistic exchange interactions and the corresponding data obtained by replacing Bi with Sb and Se with Te (no structural relaxation performed). (c) Spin-polarized PDOS of the V-3*d* states in DFT, as calculated via RSPt, with the Fermi level at zero energy. (d) Spin-polarized PDOS of the Cr-3*d* states in DFT, as calculated via RSPt, with the Fermi level at zero energy. In the inset, a comparison is made between this PDOS and the corresponding PDOS obtained by replacing Bi with Sb and Se with Te (no structural relaxation performed).

the same as for 100% doping, and thus the NN coupling is expected to be close to what discussed above. The main difference is expected for the third-neighbor exchange. While for 100% doping of the magnetic Bi layer we only have one type of third-neighbor exchange path, namely, TM-Se-TM-Se-TM/E_3, for 50% doping we have also one additional path, namely TM-Se-Bi-Se-TM/E_3'. The second-neighbor exchange path E_2 is also qualitatively different for 50% doping due to the presence of heavy Bi atoms nearby. Our aim in this case is to check how the magnetic exchange along E_3' differs from the one along E_3. Especially, along E_3' we have the direct presence of the Bi atom that could produce significant effects due to SOC. Analyzing these features will allow us to directly check the importance of the van Vleck exchange mechanism, which was instead quenched from the outset for 100% doping of the magnetic Bi layer. Since our goals also include the analysis of the structural distortions, the structures for 50% doping of the magnetic Bi layer were again fully optimized in VASP. The details of the structural changes are given in the SM [71]. The most visible structural change is the increase in the unit cell volume when the doping of the magnetic Bi layer is reduced from 100% to 50%, which is the result of a higher Bi content. The unit cell volume and lattice parameters seem almost independent from the type of TM atom. This is qualitatively different from what observed for 100% doping of the magnetic Bi layer, and may be understood by the fact that the overall concentration of dopants in the three-formula-unit conventional cell is now rather low, and in this regime the volumetric properties shall depend more on the host than on on the dopants. For simplicity, we are going to focus only on electronic structure calculations made in DFT, without additional Hubbard-like terms.

We start by investigating V and Cr systems. The calculated interatomic exchange interactions and PDOS of the TM-3*d* states are shown in Fig. 5. The spectral properties of both systems are similar to what observed for 100% doping of the magnetic Bi layer, which is expected since the TM atoms mainly bond with the Se atoms in adjacent planes [26]. Thus, the nominal oxidation states can be considered unchanged. For V, we again have a finite contribution from the T_{2g}-up

states at the Fermi level; see Fig. 5(c). For Cr, we have the same insulating solution as for 100% doping; see Fig. 5(d). The exchange coupling between magnetic moments at V sites, as a function of the V-V distance is shown in Fig. 5(a). When comparing with 100% doping of the magnetic Bi layer, shown in Fig. 2(a), we see that the NN FM interaction is very similar and comes from the combination of $T_{2g} - T_{2g}$ double exchange and $E_g - T_{2g}$ superexchange. Conversely, the second-neighbor interaction, along E_2, and one type of third-neighbor interaction (along E_3') show larger FM contributions. The presence of Bi atoms along these paths may suggest that the van Vleck mechanism plays a primary role here. However, calculations performed with SOC (green squares) show that this hypothesis is not true and a different mechanism is operating. If we now inspect the exchange coupling among Cr dopants, shown in Fig. 5(b), we do not see these FM interactions arising from the second and third neighbors. Overall, the exchange interactions for 50% doping of the magnetic Bi layer are very similar to those for 100% doping, shown in Fig. 2(b). This qualitative difference between V and Cr at 50% doping of the magnetic Bi layer is at first puzzling, since the exchange paths for both types of dopants are exactly the same. However, the analysis of the orbital components further shows that these interactions come only from the $T_{2g} - T_{2g}$ component, depicted as left triangles in Fig. 5(a). This clarifies that the origin of this coupling is not the van Vleck mechanism but the short-range double exchange mechanism. In the Cr case, this mechanism is not active, due to the insulating nature of the system, and thus we only see the NN FM superexchange. The second- and third-neighbor interactions between Cr moments instead show a weak AFM nature. This is not something new, as it was previously reported for Cr-doped Bi_2Se_3 [33], in good agreement with our results. In Refs. [33,34], the second- and third-neighbor interactions for Cr are interpreted as occurring from a polarized p-orbital network of the host without being affected by SOC. The AFM character of the exchange coupling was linked to the properties of the Se-p orbitals of the Bi_2Se_3 host and was found to become FM when Cr was doped in Bi_2Te_3 and Sb_2Te_3. To verify this speculation, we performed a calculation for the Cr system where we replaced Bi_2Se_3 with Sb_2Te_3 while keeping the structural degrees of freedom unchanged. This would allow us to focus on the changes of the $p - d$ hybridization due to the chemical species only. The resulting electronic structure and exchange parameters are shown in the inset of Figs. 5(d) and 5(b), respectively. We see that the system still remains insulating preventing the carrier-mediated mechanisms (double exchange, RKKY) from occurring. The second-neighbor and third-neighbor exchange show a marked difference with respect to the original Cr-doped Bi_2Se_3, as expected. These terms do not become FM as in Refs. [33,34] due to the lack of structural relaxation. These changes confirm the active role of the p-orbital network of the host in mediating distant exchange interactions which is much weaker compared to the carrier-driven mechanisms. The overall behavior is consistent with the Bloembergen-Rowland exchange associated to interband contributions in the absence of free carriers [42].

We can further comment on the effect of SOC. Although we see no radical change on the exchange along E_2, E_3, and E_3', the NN exchange for 50% doping of the magnetic Bi layer shows more noticeable effects due to SOC than for 100% doping. We interpret this as an indirect effect due to the fact that the Se atoms mediating the exchange coupling are now also bonded with the heavy Bi atoms. Overall, from our results, we can conclude that the van Vleck mechanism does not have any role in the magnetic coupling of V- and Cr-doped systems.

Next, we focus on Mn- and Fe-doped systems. As shown in Fig. 6(c), the magnetic moments at the Mn sites and the PDOS of the Mn-3d states are very similar to those discussed for 100% doping of the magnetic Bi layer. The hole state at the Fermi level acquires a larger spectral weight, suggesting a more delocalized nature. This increases the hole-mediated $E_g - E_g$ double exchange component, which becomes dominant over the AFM superexchange components, making the net NN exchange weakly FM. To emphasize this behavior, the $E_g - E_g$ component is also shown explicitly in Fig. 6(a) with red up-triangles. We can see a contribution to the third-neighbor exchange along the exchange path E_3', similarly to what observed for V. The most interesting changes observed for 50% doping of the magnetic Bi layer happen for Fe. As shown in Fig. 6(d), the magnetic moment at the Fe sites and the PDOS of the Fe-3d states are very different compared to 100% doping. In the spin-up channel, the hole state at the Fermi level has practically disappeared and almost no states are visible in the unoccupied part of the spectrum. As a result, the hole-mediated $E_g - E_g$ double exchange is no longer active, as shown in Fig. 6(b). The contribution from the T_{2g}-dn state at the Fermi level is also reduced significantly, which quenches the short-ranged FM $T_{2g} - T_{2g}$ double exchange discussed for 100% doping. Although a small number of T_{2g} states at the Fermi level induces a very weak long-ranged oscillation in the exchange coupling, the stronger AFM NN value cannot come from RKKY mechanism. Since Fig. 6(d) shows an almost insulating system, the NN $T_{2g} - T_{2g}$ exchange may be due to the direct exchange mechanism or to the superexchange mechanism. In any case, due to the small finite contribution of T_{2g}-dn and, to a lesser extent, E_g-up states at the Fermi level, the AFM double exchange type $E_g - T_{2g}$ component remains as before, giving rise to the dominant AFM NN exchange.

To further check and verify the nature of the exchange interaction, we again modeled an AFM ordering of the Fe atoms, which is shown in Fig. 7(a). A significant difference between this system and the one shown in Fig. 4(c) is that in this case we have no lattice frustration and therefore we expect this system to arise naturally from the exchange interactions plotted in Fig. 6(b). The total energy of the AFM solution comes out to be lower than the FM solution, as expected from the exchange coupling. The calculated total DOS and PDOS of the Fe-3d states for this AFM state are shown in Fig. 7(b). The total and orbitally decomposed exchange parameters as a function of the Fe-Fe distance are shown in Fig. 7(c). As can be seen from the DOS, the system looks insulating with no contribution at E_F from the Fe-3d states in the majority spin channel. A small spectral weight from the T_{2g}-dn states is visible, but this is only due to the Lorentzian smearing used for printing the spectral properties via Green's function theory [72]. This can be immediately verified by looking at the DOS calculated for a smaller smearing, shown in the inset of Fig. 7(b). It is interesting to see how this drastic change

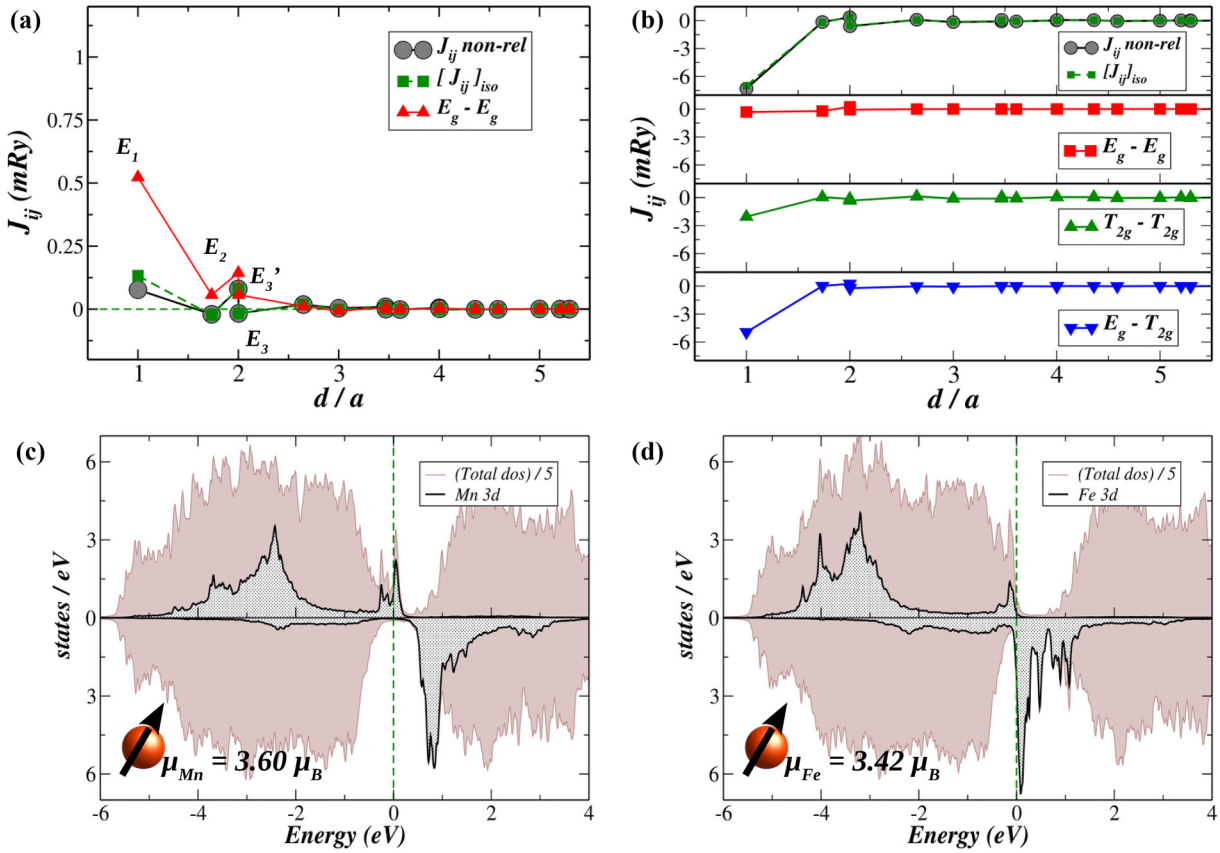

FIG. 6. (a) Orbital-resolved interatomic exchange interactions between magnetic moments at the Mn sites in Mn-doped Bi_2Se_3 for 50% doping of the magnetic Bi layer, as a function of the Mn-Mn distance. Calculations made with RSPt in DFT, without and with SOC. For the latter, only the total isotropic averages of the exchange tensor are plotted (green squares). (b) Orbital-resolved interatomic exchange interactions between magnetic moments at the Fe sites in Fe-doped Bi_2Se_3 for 50% doping of the magnetic Bi layer, as a function of the Fe-Fe distance. Calculations made with RSPt in DFT, without and with SOC. For the latter, only the total isotropic averages of the exchange tensor are plotted (green squares). (c) Spin-polarized total DOS and PDOS of the Mn-3*d* states in DFT, as calculated via RSPt, with the Fermi level at zero energy. The total magnetic moment at the Mn site is also indicated. (d) Spin-polarized total DOS and PDOS of the Fe-3*d* states in DFT, as calculated via RSPt, with the Fermi level at zero energy. The total magnetic moment at the Fe site is also indicated.

in the conducting character affects the calculated exchange coupling. As seen in Fig. 7(c), the $E_g - E_g$ component is again zero, as expected. The $E_g - T_{2g}$ exchange is now suppressed, since the transition to an insulator makes the AFM double exchange no longer possible. The $T_{2g} - T_{2g}$ NN AFM interaction remains almost unaffected, but the weak long-ranged

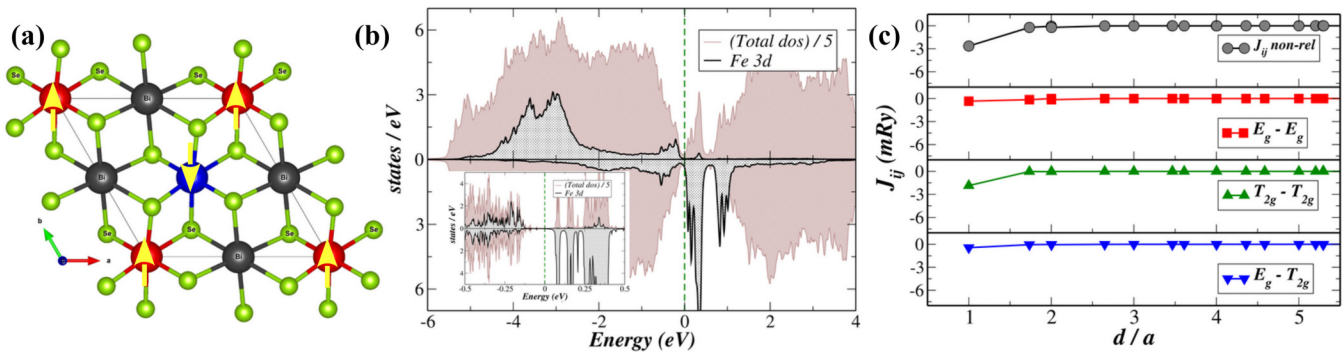

FIG. 7. (a) A sketch of the AFM ordering of the Fe atoms assumed for 50% doping of the magnetic Bi layer, as discussed in the main text. (b) Spin-polarized total DOS and PDOS of the Fe-3*d* states of the AFM system shown in (a), as calculated in DFT via RSPt, with the Fermi level at zero energy. The inset shows the magnified region around the Fermi level where the Lorentzian smearing has been decreased to a point where the gap formation can be resolved. (c) Orbital-resolved inter-atomic exchange interactions between magnetic moments at the Fe sites in the AFM system shown in (a), as a function of the Fe-Fe distance. Calculations made with RSPt in DFT, without SOC.

oscillatory part that is visible in Fig. 6(b) has now vanished. This demonstrates that the NN AFM exchange cannot be due to the RKKY interaction, but is most likely caused by the superexchange mechanism or by the direct exchange mechanism, as guessed above. However, the Se atoms in our structure are not arranged to form the Fe-Se-Fe 180° exchange path that is necessary to produce a strong AFM superexchange. Therefore, the NN AFM $T_{2g} - T_{2g}$ term is most likely caused by the direct exchange between the neighboring Fe atoms. We can speculate that this contribution is also present for 100% doping of the magnetic Bi layer, but gets outweighed by the carrier-mediated double exchange or RKKY mechanisms. These terms are not only present in the FM state, but also in the AFM state, see Fig. 4(d), which is a consequence of the closely spaced Fe atoms on a triangular lattice. We should keep in mind that our model of the AFM did not include noncollinearity, which is likely to emerge in a frustrated lattice. We can speculate that a noncollinear magnetic order may induce a transition to an insulator, thus making the NN direct exchange the dominating interaction. Hence we can conclude that Fe exhibits a very complex competition of exchange mechanisms, whose balance is expected to depend strongly on the doping concentration and on the nature of the host affecting the subtle details of the $p - d$ hybridization. At a methodological level, this is the system where we expect the stronger dependence of the results on the choice of the computational approach. Investigating the evolution of the magnetic coupling of Fe in the dilute limit, as well as the role played by strong electronic correlations seems, an interesting plan for future research.

VI. CONCLUSION

Taking advantage of the local octahedral symmetry, we have investigated the nature of the intraplane exchange coupling in TM-doped Bi_2Se_3. We have calculated the orbital-decomposed exchange interactions between TM atoms replacing Bi atoms in a single layer inside a single QL in the three-formula-unit hexagonal conventional cells for two different concentrations (full coverage and half coverage). Correlating the interatomic exchange interactions with the calculated electronic structure, we are able to directly identify the various types of exchange mechanisms that have been discussed in the literature so far. A variation of the Coulomb interaction parameter U in DFT + U provides further insight into the electronic and magnetic response, enriching our analysis. Even if our 2D model may seem an oversimplification at first, our calculations demonstrate that it is capable to capture all the features of the in-plane exchange coupling that have been identified by recent literature. This result is interpreted as a consequence of the key role played by the covalent bond between transition metal atoms and selenium in supporting the magnetism. In agreement with several other studies, we conclude that the van Vleck mechanism does not play a significant role in the magnetic order [27,32–35,42]. As predicted by a recent work on Mn-doped HgTe [42], superexchange is found to be very important in determining the properties of TM-doped tetradymite semiconductors, and competition with other exchange mechanisms depends crucially on the filling of the TM-3d shell. In disagreement with the same study [42], we instead demonstrate that the double-exchange mechanism cannot be ignored, since it plays a major role for various elements. This may be a consequence of their speculations being based on the electronic structure determined in DFT + U for a larger value of U than the one adopted in our work. Alternatively, considering that the localization of the 3d states is supposed to increase in the dilute limit, we cannot exclude that our conclusion depends on the particular regime of doping chosen for our calculations, although it seems unlikely if we look at the strength of the covalent bond between TM and Se.

Going into detail, we find that Cr is the only system that shows an insulating state which is robust against a change of doping concentration and Hubbard U. For such a system, the exchange interaction is short-range and driven by the superexchange mechanism. Instead, V, Mn, and Fe show a finite carrier density, which opens the possibility of carrier-mediated exchange mechanisms. For V, the driving mechanism is the strong, electron-mediated double exchange, which in combination with the superexchange causes a strong, short-range FM coupling. For Mn, AFM superexchange competes with a hole-mediated FM double exchange, resulting in an almost zero magnetic coupling. For Fe, a more intriguing combination of short-range and long-range contributions can be observed. Our calculations show a complex interplay between various exchange mechanisms, whose balance depends crucially on the doping concentration, details of the host, and computational method used. The high tunability of the various short- and long-range exchange mechanisms makes Fe the most interesting system for further studies with more complex methods, as, e.g., aimed at the description of strong electronic correlations or at the formation of complex magnetic textures.

A final comment has to be made on the description of the oxidation state. In the present paper, we employed the electronic charges projected on atomiclike orbitals to argue in favor of a 2+ oxidation state. This analysis is in agreement with available core-level spectroscopy, but in disagreement with speculations based on the magnetic moments expected from Hund's rules. Although the very concept of oxidation state is poorly defined in solids, focusing on electronic charges alone may not be an ideal choice [104]. A more rigorous analysis may be provided by using the modern theory of polarization, at least for those systems that have a robust insulating nature [105]. Alternatively, one may employ a counting scheme based on the construction of maximally localized Wannier functions [106]. A more detailed analysis of the oxidation state of TM-doped Bi_2Se_3 plays no role in the discussion of the exchange mechanism presented in this paper, but is important for the construction of realistic magnetic models as well as for the interpretation of experimental data.

ACKNOWLEDGMENTS

The computational work was enabled by resources provided by the National Academic Infrastructure for Supercomputing in Sweden (NAISS), partially funded by the Swedish Research Council through Grant Agreement No. 2022-06725 and by the Swedish National Infrastructure for Computing (SNIC) partially funded by the Swedish Research Council through Grant Agreement No. 2018-05973. Supercomputers were provided at the Center for High

Performance Computing (PDC) in Stockholm, Sweden, and at the National Supercomputer Centre (NSC) of Linköping University, Sweden. This study was financially supported by the National Research Foundation (NRF) of Korea, Grant No. 2020R1A2C101217411, funded by the Korean government through the Ministry of Science and Technology Information and Communication (MSIT). The work of I.D.M. was also supported by the appointment to the JRG program at the APCTP through the Science and Technology Promotion Fund and Lottery Fund of the Korean Government, as well as by the Korean Local Governments, Gyeongsangbuk-do Province, and Pohang City. O.E. and I.D.M. acknowledge further financial support from the European Research Council (ERC), Synergy Grant FASTCORR, Project No. 854843. O.E. also acknowledges support from the Wallenberg Initiative Materials Science for Sustainability (WISE) funded by the Knut and Alice Wallenberg Foundation, as well as from eSSENCE, and STandUPP.

[1] K. v. Klitzing, G. Dorda, and M. Pepper, Phys. Rev. Lett. **45**, 494 (1980).
[2] C.-X. Liu, X.-L. Qi, X. Dai, Z. Fang, and S.-C. Zhang, Phys. Rev. Lett. **101**, 146802 (2008).
[3] J. Wu, J. Liu, and X.-J. Liu, Phys. Rev. Lett. **113**, 136403 (2014).
[4] F. D. M. Haldane, Phys. Rev. Lett. **61**, 2015 (1988).
[5] R. Yu, W. Zhang, H.-J. Zhang, S.-C. Zhang, X. Dai, and Z. Fang, Science **329**, 61 (2010).
[6] R.-X. Zhang, H.-C. Hsu, and C.-X. Liu, Phys. Rev. B **93**, 235315 (2016).
[7] H. Zhang, C.-X. Liu, X.-L. Qi, X. Dai, Z. Fang, and S.-C. Zhang, Nat. Phys. **5**, 438 (2009).
[8] C.-Z. Chang, J. Zhang, X. Feng, J. Shen, Z. Zhang, M. Guo, K. Li, Y. Ou, P. Wei, L.-L. Wang *et al.*, Science **340**, 167 (2013).
[9] X. Kou, S.-T. Guo, Y. Fan, L. Pan, M. Lang, Y. Jiang, Q. Shao, T. Nie, K. Murata, J. Tang *et al.*, Phys. Rev. Lett. **113**, 137201 (2014).
[10] J. Checkelsky, R. Yoshimi, A. Tsukazaki, K. Takahashi, Y. Kozuka, J. Falson, M. Kawasaki, and Y. Tokura, Nat. Phys. **10**, 731 (2014).
[11] A. J. Bestwick, E. J. Fox, X. Kou, L. Pan, K. L. Wang, and D. Goldhaber-Gordon, Phys. Rev. Lett. **114**, 187201 (2015).
[12] C.-Z. Chang, W. Zhao, D. Y. Kim, H. Zhang, B. A. Assaf, D. Heiman, S.-C. Zhang, C. Liu, M. H. Chan, and J. S. Moodera, Nat. Mater. **14**, 473 (2015).
[13] C.-Z. Chen, Y.-M. Xie, J. Liu, P. A. Lee, and K. T. Law, Phys. Rev. B **97**, 104504 (2018).
[14] Y. Feng, X. Feng, Y. Ou, J. Wang, C. Liu, L. Zhang, D. Zhao, G. Jiang, S.-C. Zhang, K. He *et al.*, Phys. Rev. Lett. **115**, 126801 (2015).
[15] C.-Z. Chang, C.-X. Liu, and A. H. MacDonald, Rev. Mod. Phys. **95**, 011002 (2023).
[16] Y. Ou, C. Liu, G. Jiang, Y. Feng, D. Zhao, W. Wu, X.-X. Wang, W. Li, C. Song, L.-L. Wang *et al.*, Adv. Mater. **30**, 1703062 (2018).
[17] M. Mogi, R. Yoshimi, A. Tsukazaki, K. Yasuda, Y. Kozuka, K. S. Takahashi, M. Kawasaki, and Y. Tokura, Appl. Phys. Lett. **107**, 182401 (2015).
[18] Z. Zhou, Y.-J. Chien, and C. Uher, Appl. Phys. Lett. **87**, 112503 (2005).
[19] Z. Zhou, Y.-J. Chien, and C. Uher, Phys. Rev. B **74**, 224418 (2006).
[20] Y. Tokura, K. Yasuda, and A. Tsukazaki, Nat. Rev. Phys. **1**, 126 (2019).
[21] J. H. Van Vlek, *The Theory of Electric and Magnetic Susceptibilities—Scholar's Choice Edition* (Bibliolife DBA of Bibilio Bazaar II LLC, Charleston, South Carolina, 2015).
[22] C.-Z. Chang, J. Zhang, M. Liu, Z. Zhang, X. Feng, K. Li, L.-L. Wang, X. Chen, X. Dai, Z. Fang *et al.*, Adv. Mater. **25**, 1065 (2013).
[23] M. Li, C.-Z. Chang, L. Wu, J. Tao, W. Zhao, M. H. W. Chan, J. S. Moodera, J. Li, and Y. Zhu, Phys. Rev. Lett. **114**, 146802 (2015).
[24] T. R. F. Peixoto, H. Bentmann, S. Schreyeck, M. Winnerlein, C. Seibel, H. Maaß, M. Al-Baidhani, K. Treiber, S. Schatz, S. Grauer *et al.*, Phys. Rev. B **94**, 195140 (2016).
[25] M. Ye, T. Xu, G. Li, S. Qiao, Y. Takeda, Y. Saitoh, S.-Y. Zhu, M. Nurmamat, K. Sumida, Y. Ishida *et al.*, Phys. Rev. B **99**, 144413 (2019).
[26] A. Tcakaev, V. B. Zabolotnyy, R. J. Green, T. R. F. Peixoto, F. Stier, M. Dettbarn, S. Schreyeck, M. Winnerlein, R. C. Vidal, S. Schatz *et al.*, Phys. Rev. B **101**, 045127 (2020).
[27] M. G. Vergniory, M. M. Otrokov, D. Thonig, M. Hoffmann, I. V. Maznichenko, M. Geilhufe, X. Zubizarreta, S. Ostanin, A. Marmodoro, J. Henk *et al.*, Phys. Rev. B **89**, 165202 (2014).
[28] P. Rüßmann, S. K. Mahatha, P. Sessi, M. A. Valbuena, T. Bathon, K. Fauth, S. Godey, A. Mugarza, K. A. Kokh, O. E. Tereshchenko *et al.*, J. Phys. Mater. **1**, 015002 (2018).
[29] Z. Zhang, X. Feng, M. Guo, K. Li, J. Zhang, Y. Ou, Y. Feng, L. Wang, X. Chen, K. He *et al.*, Nat. Commun. **5**, 4915 (2014).
[30] M. Ye, W. Li, S. Zhu, Y. Takeda, Y. Saitoh, J. Wang, H. Pan, M. Nurmamat, K. Sumida, F. Ji *et al.*, Nat. Commun. **6**, 8913 (2015).
[31] F. Wang, Y.-F. Zhao, Z.-J. Yan, D. Zhuo, H. Yi, W. Yuan, L. Zhou, W. Zhao, M. H. W. Chan, and C.-Z. Chang, Nano Lett. **23**, 2483 (2023).
[32] P. Larson and W. R. L. Lambrecht, Phys. Rev. B **78**, 195207 (2008).
[33] J. Kim, S.-H. Jhi, A. H. MacDonald, and R. Wu, Phys. Rev. B **96**, 140410(R) (2017).
[34] J. Kim, H. Wang, and R. Wu, Phys. Rev. B **97**, 125118 (2018).
[35] T. R. Peixoto, H. Bentmann, P. Rüßmann, A.-V. Tcakaev, M. Winnerlein, S. Schreyeck, S. Schatz, R. C. Vidal, F. Stier, V. Zabolotnyy *et al.*, npj Quantum Mater. **5**, 87 (2020).
[36] T. Dietl, A. Haury, and Y. Merle d'Aubigné, Phys. Rev. B **55**, R3347 (1997).
[37] T. Dietl, H. Ohno, F. Matsukura, J. Cibert, and D. Ferrand, Science **287**, 1019 (2000).
[38] K. Sato, L. Bergqvist, J. Kudrnovský, P. H. Dederichs, O. Eriksson, I. Turek, B. Sanyal, G. Bouzerar, H. Katayama-Yoshida, V. A. Dinh *et al.*, Rev. Mod. Phys. **82**, 1633 (2010).
[39] T. Dietl, Nat. Mater. **9**, 965 (2010).
[40] T. Dietl and H. Ohno, Rev. Mod. Phys. **86**, 187 (2014).
[41] N. Bloembergen and T. J. Rowland, Phys. Rev. **97**, 1679 (1955).

[42] C. Śliwa, C. Autieri, J. A. Majewski, and T. Dietl, Phys. Rev. B **104**, L220404 (2021).

[43] J. Kim and S.-H. Jhi, Phys. Rev. B **92**, 104405 (2015).

[44] K. Lejaeghere, G. Bihlmayer, T. Björkman, P. Blaha, S. Blügel, V. Blum, D. Caliste, I. E. Castelli, S. J. Clark, A. D. Corso *et al.*, Science **351**, aad3000 (2016).

[45] V. I. Anisimov, F. Aryasetiawan, and A. I. Lichtenstein, J. Phys.: Condens. Matter **9**, 767 (1997).

[46] G. Kotliar, S. Y. Savrasov, K. Haule, V. S. Oudovenko, O. Parcollet, and C. A. Marianetti, Rev. Mod. Phys. **78**, 865 (2006).

[47] Y. O. Kvashnin, R. Cardias, A. Szilva, I. Di Marco, M. I. Katsnelson, A. I. Lichtenstein, L. Nordström, A. B. Klautau, and O. Eriksson, Phys. Rev. Lett. **116**, 217202 (2016).

[48] P. E. Blöchl, Phys. Rev. B **50**, 17953 (1994).

[49] G. Kresse and D. Joubert, Phys. Rev. B **59**, 1758 (1999).

[50] G. Kresse and J. Hafner, Phys. Rev. B **47**, 558 (1993).

[51] G. Kresse and J. Hafner, Phys. Rev. B **49**, 14251 (1994).

[52] G. Kresse and J. Furthmüller, Phys. Rev. B **54**, 11169 (1996).

[53] G. Kresse and J. Furthmüller, Comput. Mater. Sci. **6**, 15 (1996).

[54] P. A. M. Dirac, Math. Proc. Cambridge Philos. Soc. **26**, 376 (1930).

[55] D. M. Ceperley and B. J. Alder, Phys. Rev. Lett. **45**, 566 (1980).

[56] J. P. Perdew and A. Zunger, Phys. Rev. B **23**, 5048 (1981).

[57] J. P. Perdew, K. Burke, and M. Ernzerhof, Phys. Rev. Lett. **77**, 3865 (1996).

[58] J. P. Perdew, K. Burke, and M. Ernzerhof, Phys. Rev. Lett. **78**, 1396(E) (1997).

[59] S. Grimme, J. Comput. Chem. **27**, 1787 (2006).

[60] K. Shirali, W. A. Shelton, and I. Vekhter, J. Phys.: Condens. Matter **33**, 035702 (2021).

[61] S. Steiner, S. Khmelevskyi, M. Marsmann, and G. Kresse, Phys. Rev. B **93**, 224425 (2016).

[62] H. J. Monkhorst and J. D. Pack, Phys. Rev. B **13**, 5188 (1976).

[63] A. I. Liechtenstein, V. I. Anisimov, and J. Zaanen, Phys. Rev. B **52**, R5467 (1995).

[64] MF. Islam, C. M. Canali, A. Pertsova, A. Balatsky, S. K. Mahatha, C. Carbone, A. Barla, K. A. Kokh, O. E. Tereshchenko, E. Jiménez, N. B. Brookes, P. Gargiani, M. Valvidares, S. Schatz, T. R. F. Peixoto, H. Bentmann, F. Reinert, J. Jung, T. Bathon, K. Fauth, M. Bode, and P. Sessi, Phys. Rev. B **97**, 155429 (2018).

[65] K. Yang, F. Fan, H. Wang, D. I. Khomskii, and H. Wu, Phys. Rev. B **101**, 100402(R) (2020).

[66] J. M. Wills, M. Alouani, P. Andersson, A. Delin, O. Eriksson, and O. Grechnyev, *Full-Potential Electronic Structure Method: Energy and Force Calculations with Density Functional and Dynamical Mean Field Theory* (Springer Science & Business Media, Berlin, 2010), Vol. 167.

[67] https://www.physics.uu.se/research/materials-theory/ongoing-research/code-development/rspt-main/, source RSPt.

[68] J. P. Perdew and Y. Wang, Phys. Rev. B **45**, 13244 (1992).

[69] R. Armiento and A. E. Mattsson, Phys. Rev. B **72**, 085108 (2005).

[70] M. Kodera, T. Shishidou, and T. Oguchi, J. Phys. Soc. Jpn. **79**, 074713 (2010).

[71] See Supplemental Material at http://link.aps.org/supplemental/10.1103/PhysRevB.110.064412 for additional details on the calculations, as well as the results of the optimized lattice parameters and elastic properties.

[72] O. Grånäs, I. Di Marco, P. Thunström, L. Nordström, O. Eriksson, T. Björkman, and J. Wills, Comput. Mater. Sci. **55**, 295 (2012).

[73] A. Grechnev, I. Di Marco, M. I. Katsnelson, A. I. Lichtenstein, J. Wills, and O. Eriksson, Phys. Rev. B **76**, 035107 (2007).

[74] Y. O. Kvashnin, O. Grånäs, I. Di Marco, M. I. Katsnelson, A. I. Lichtenstein, and O. Eriksson, Phys. Rev. B **91**, 125133 (2015).

[75] A. Szilva, Y. Kvashnin, E. A. Stepanov, L. Nordström, O. Eriksson, A. I. Lichtenstein, and M. I. Katsnelson, Rev. Mod. Phys. **95**, 035004 (2023).

[76] A. Liechtenstein, M. Katsnelson, V. Antropov, and V. Gubanov, J. Magn. Magn. Mater. **67**, 65 (1987).

[77] A. I. Lichtenstein and M. I. Katsnelson, Phys. Rev. B **62**, R9283 (2000).

[78] R. Cardias, A. Szilva, A. Bergman, I. Di Marco, M. Katsnelson, A. Lichtenstein, L. Nordström, A. Klautau, O. Eriksson, and Y. O. Kvashnin, Sci. Rep. **7**, 1 (2017).

[79] Y. O. Kvashnin, A. Bergman, A. I. Lichtenstein, and M. I. Katsnelson, Phys. Rev. B **102**, 115162 (2020).

[80] T. Moriya, Phys. Rev. **120**, 91 (1960).

[81] I. Dzyaloshinsky, J. Phys. Chem. Solids **4**, 241 (1958).

[82] S. Nakajima, J. Phys. Chem. Solids **24**, 479 (1963).

[83] J. Horák, Z. Stary, P. Lošťák, and J. Pancíř, J. Phys. Chem. Solids **51**, 1353 (1990).

[84] C. Pérez Vicente, J. Tirado, K. Adouby, J. Jumas, A. A. Touré, and G. Kra, Inorg. Chem. **38**, 2131 (1999).

[85] S. Grimme, J. Antony, S. Ehrlich, and H. Krieg, J. Chem. Phys. **132**, 154104 (2010).

[86] K. Carva, P. Baláž, J. Šebesta, I. Turek, J. Kudrnovský, F. Máca, V. Drchal, J. Chico, V. Sechovský, and J. Honolka, Phys. Rev. B **101**, 054428 (2020).

[87] S. Sarkar, O. Eriksson, D. D. Sarma, and I. Di Marco, Phys. Rev. B **105**, 184201 (2022).

[88] S. Nahas, B. Sanyal, and A. M. Black-Schaffer, Phys. Rev. B **102**, 140407(R) (2020).

[89] J. Zhang, C.-Z. Chang, P. Tang, Z. Zhang, X. Feng, K. Li, L. li Wang, X. Chen, C. Liu, W. Duan *et al.*, Science **339**, 1582 (2013).

[90] Y.-F. Zhao, R. Zhang, R. Mei, L.-J. Zhou, H. Yi, Y.-Q. Zhang, J. Yu, R. Xiao, K. Wang, N. Samarth *et al.*, Nature (London) **588**, 419 (2020).

[91] M.-C. Wang and C.-R. Chang, J. Electrochem. Soc. **169**, 053507 (2022).

[92] T. Jungwirth, J. Sinova, J. Mašek, J. Kučera, and A. H. MacDonald, Rev. Mod. Phys. **78**, 809 (2006).

[93] H. Wang, F. Fan, S. Zhu, and H. Wu, Europhys. Lett. **114**, 47001 (2016).

[94] F. Xue, Y. Hou, Z. Wang, and R. Wu, Phys. Rev. B **100**, 224429 (2019).

[95] Y. H. Choi, N. H. Jo, K. J. Lee, H. W. Lee, Y. H. Jo, J. Kajino, T. Takabatake, K.-T. Ko, J.-H. Park, and M. H. Jung, Appl. Phys. Lett. **101**, 152103 (2012).

[96] Y. Li, X. Zou, J. Li, and G. Zhou, J. Chem. Phys. **140**, 124704 (2014).

[97] N. Almeleh and B. Goldstein, Phys. Rev. **128**, 1568 (1962).
[98] J. Szczytko, A. Twardowski, K. Świątek, M. Palczewska, M. Tanaka, T. Hayashi, and K. Ando, Phys. Rev. B **60**, 8304 (1999).
[99] I. Di Marco, P. Thunström, M. I. Katsnelson, J. Sadowski, K. Karlsson, S. Lebègue, J. Kanski, and O. Eriksson, Nat. Commun. **4**, 2645 (2013).
[100] J. Fujii, B. R. Salles, M. Sperl, S. Ueda, M. Kobata, K. Kobayashi, Y. Yamashita, P. Torelli, M. Utz, C. S. Fadley *et al.*, Phys. Rev. Lett. **111**, 097201 (2013).
[101] Y. Sasaki, X. Liu, J. K. Furdyna, M. Palczewska, J. Szczytko, and A. Twardowski, J. Appl. Phys. **91**, 7484 (2002).
[102] H. C. Herper, T. Ahmed, J. M. Wills, I. Di Marco, T. Björkman, D. Iuşan, A. V. Balatsky, and O. Eriksson, Phys. Rev. Mater. **1**, 033802 (2017).
[103] R. Cardias, A. Szilva, M. M. Bezerra-Neto, M. S. Ribeiro, A. Bergman, Y. O. Kvashnin, J. Fransson, A. B. Klautau, O. Eriksson, and L. Nordström, Sci. Rep. **10**, 20339 (2020).
[104] A. Walsh, A. A. Sokol, J. Buckeridge, D. O. Scanlon, and C. R. A. Catlow, Nat. Mater. **17**, 958 (2018).
[105] L. Jiang, S. V. Levchenko, and A. M. Rappe, Phys. Rev. Lett. **108**, 166403 (2012).
[106] Y. Quan and W. E. Pickett, Phys. Rev. B **91**, 035121 (2015).